Platelets regulate glioblastoma growth and immunity via sex-dependent PAR4 - Estrogen receptor beta signaling

Anthony R. Sloan[1,2], George Bukenya[1], Gavin P. Tannish[1], Daniel J. Silver[1,2,3], Anu Aggarwal[4], Juyeun Lee[1,2], Daniel Rosoff[5,6], Tyler J. Alban[1,2,3], Ivan Juric[1,5], Shikha Parsai[1,5], Vargab Baruah[7], Liza Tack[1], Tanvi Navadgi[1], Natalie Reitz[1], Shawn T. Ho[2,9], Aarav Badani[1], Jessica Goldberg[1], Xueer Yuan[1], Aymerick Gaboriau[1], Samrutha Kamatala[1], Jesse Coker[2,3], Vrishabhadev Sathish Kumar[2,9], Saachi S. Jain[2,9], Alliefair Scalise[4,10,11], Bhairavi Rajasekar[4,10,11], Alex Vincenti[1], Erin E. Mulkearns-Hubert[1,2,3], Craig M. Horbinski[12], Andrew E. Sloan[13], Christopher G. Hubert[2,14], Jingqin Luo[15], Joshua B. Rubin[16,17], Evi X. Stavrou[2,18,19], Falk W. Lohoff[5,6], Wendy A. Goodman[2,9], Tyler E. Miller[2,9], Christine M. O'Connor[2,3,7], Marvin T. Nieman[2,20], Naseer Sangwan[4], Timothy A. Chan[1,2,3,21,22], Alok A. Khorana[2,3,4,21], Andrew Dhawan[1,2,3,22], Scott J. Cameron[4,9,11], Justin D. Lathia[1,2,3,22]

Departments of [1]Cancer Sciences and [4]Heart, Blood, and Kidney Research, [7]Microbial Sciences, [8]Sheika Fatima bint Mubarak Global Center for Pathogen and Human Health Research, Cleveland Clinic Research, Cleveland Clinic, Cleveland, Ohio, USA

[2]Case Comprehensive Cancer Center, Cleveland, Ohio, USA

[3]Cleveland Clinic Lerner College of Medicine of Case Western Reserve University, Cleveland, Ohio, USA

[5]Section on Clinical Genomics and Experimental Therapeutics, National Institute on Alcohol Abuse and Alcoholism, National Institutes of Health, Bethesda, Maryland, USA

[6]NIH Oxford-Cambridge Scholars Program, National Institutes of Health, Bethesda, Maryland, USA

Departments of [9]Pathology, [14]Biochemistry, [19]Medicine, Hematology and Oncology Division, and [20]Pharmacology, Case Western Reserve University School of Medicine, Cleveland, Ohio, USA

[10]Department of Cardiovascular Medicine, Section of Vascular Medicine, Cleveland Clinic, Cleveland, Ohio, USA

[11]Heart Vascular and Thoracic Institute, Department of Cardiovascular Medicine, Section of Vascular Medicine, Cleveland Clinic, Cleveland, Ohio, USA

[12]Departments of Laboratory Medicine and Pathology, Mayo Clinic Florida, Jacksonville, Florida.

[13]Neuroscience Institute and Department of Neurosurgery, Wright State University School of Medicine, Dayton, Ohio, USA

[15]Department of Surgery, Washington University School of Medicine, St. Louis, Missouri, USA

[16]Department of Pediatrics, Washington University School of Medicine, St. Louis, Missouri, USA

[17]Department of Neurosciences, Washington University School of Medicine, St. Louis, Missouri, USA

[18]Medicine Service, Section of Hematology-Oncology, Louis Stokes Veterans, Cleveland, Ohio, USA

[21]Taussig Cancer Institute, Cleveland Clinic, Cleveland, Ohio, USA

[22]Rose Ella Burkhardt Brain Tumor & Neuro-Oncology Center, Cleveland Clinic, Cleveland, Ohio, USA

Corresponding author
Justin D. Lathia
9500 Euclid Ave, NE3-202
Cleveland, OH 44195
Phone: (216) 445-7475
E-mail: lathiaj@ccf.org

Figures: 8

Abstract

Sex differences in cancer outcome, including that of glioblastoma (GBM), are shaped by biological, hormonal, and immunological factors and impact disease progression, treatment responses, survival, and tumor microenvironment (TME) interactions. Platelets regulate the immune responses and tumor progression in many cancers, but it is not clear how they contribute to these sex-based differences by affecting the dynamics of the TME. Here, we show that GBM patients exhibit heightened platelet reactivity driven by PAR4 signaling. In murine GBM models, both pharmacological inhibition of PAR4 using BMS986120 and genetic deletion of PAR4 significantly prolong survival in females but not males. This survival advantage is estrogen dependent: it is preserved in chromosomal male-hormonal female mice within the four-core genotype model and is rescued in ovariectomized mice treated with estrogen. The survival benefit is TME specific and is mediated by platelet-driven enhancement of $CD8^+$ T cell infiltration into the tumor. Inhibition of platelet PAR4 signaling increases calcium signaling through an estrogen-dependent interaction between PAR4 and estrogen receptor β (ERβ)—a receptor interaction not previously described. PAR4-activated platelets within the TME suppress $CD8^+$ T cell function, and depletion of $CD8^+$ T cells abolishes both the tumor-induced platelet reactivity and the survival benefit conferred by PAR4 inhibition. These findings establish platelet-mediated PAR4 signaling as a critical driver of tumor progression and identify sex-specific immune responses as key to therapeutic efficacy.

Introduction

Sex differences underlie and influence risk, progression, and treatment outcomes across many cancers. For example, men are more likely to develop several cancer types, including glioblastoma (GBM), while women often exhibit better survival rates[1, 2]. Despite these appreciated epidemiological differences, treatment paradigms remain uniform, highlighting the opportunity for sex-specific therapies shaped by hormonal, genetic, and immune differences. Sex differences in cancer also involve the tumor microenvironment (TME) — a complex network of cells and anatomical structures, including blood vessels, that interact with tumors. Among components of the TME, platelets play a major role in maintaining vascular integrity and modulating immune responses, potentially offering key insights into the relationship between sex differences and cancer progression. While platelets are present in the TME and known to influence immune cells, their role in cancer, particularly in thrombotic events and sex differences via thrombin-PAR4 signaling, remains underexplored[3-6]. In a recent study, the antiplatelet drug aspirin, which inhibits cyclooxygenase-1 and cyclooxygenase-2, enhanced the protective mechanism of T cells and therefore inhibited metastasis in murine models of lung and liver malignancies, further supporting the role of platelets in mediating cancer progression[7].

In GBM, the most common primary malignant brain tumor in adults, immune cells in the TME suppress anti-tumor responses. Myeloid derived supporesor cells (MDSCs) drive immune suppression in GBM, while lymphocytes, such as CD8+ T cells, are reduced and have decreased T cell function[8-10]. Moreover, GBM has a striking difference in incidence and prognosis, with men 1.6 times more likely to develop the disease and exhibiting shorter survival[2, 11]. Both intrinsic factors and immune cells such as microglia, MDSCs, and CD8+ T cells contribute to these differences[8, 10], with myeloid-derived cells having enhanced proliferation in males and male CD8+ T cells showing a greater propensity for exhaustion[10]. Although platelet-derived factors are known to promote tumor growth, their underlying mechanisms and role in sex-based differences in GBM are unclear[4, 12]. Thrombotic events, such as deep vein thrombosis (DVT) and pulmonary embolism (PE) are common in cancer patients and a leading cause of morbidity and mortality, although cause of death is not attributed to intravascular thrombosis[13, 14]. GBM patients face a 15-24% risk of thrombotic events, and patients with thrombotic events have worse outcomes, suggesting that a pro-thrombotic state drives cancer progression[15-18]. Therefore, given the sex

99 difference in the incidence and aggressiveness of GBM that is driven by an immunosuppressive
100 microenvironment more pronounced in males, we sought to determine whether sex-dependent platelet effects
101 contribute to the immunosuppressive TME in GBM.
102
103 **Results**
104
105 **PAR4 signaling drives hyperactive platelets in GBM patients**
106
107 The GBM TME shapes the trajectory of tumor growth and response to therapies. A variety of mechanisms
108 underlie TME-tumor interactions[1]; however, the role of platelets remains underappreciated. We and others have
109 previously reported that high platelet counts are temporally related to worsened clinical outcomes in patients with
110 any malignancy, including GBM[4, 19, 20]. By carefully evaluating a platelet transcriptomic signature in the context
111 of large-scale human datasets, we found that an enrichment of a platelet gene signature is associated with poor
112 overall survival in GBM patients (**Figure 1A, Figure S1A, Table S1**) and negatively correlated with several anti-
113 tumor immune cell populations including T cells, dendritic cells (DCs), and B cells (**Figure S1B, Table S2**). These
114 data indicates that platelets are a negative prognostic and immunosuppressive factor in GBM patients.
115
116 Next, we asked whether GBM patients have altered platelet physiology when compared to age- and sex-matched
117 control subjects. We measured platelet reactivity from peripheral blood using assays that measure degranulation
118 of platelet contents in GBM patients and control subjects (**Table S3, Table S4**). Platelets from both male and
119 female GBM patients had increased agonist-induced reactivity, measured my P-Selectin, due to protease-
120 activated receptor 4 (PAR4) signaling (**Figure 1B, Figure S2A-C**). However, agonist-induced platelet reactivity
121 via protease-activated receptor 1 (PAR1), thromboxane receptor (TXA2), and purinergic receptor P2Y12 was
122 similar or not as drastically different between GBM and control subjects (**Figure S2D-F**). Thrombin is a potent
123 human platelet agonist that acts via the PAR1 and PAR4 receptors and is quantified by measuring plasma levels
124 of thrombin-antithrombin (TAT) complexes. We found that GBM patients had significantly higher TAT levels
125 relative to healthy age-matched control subjects (**Figure 1C**). Consistently, *in vivo* studies utilizing murine GBM
126 models demonstrated that tumor-bearing mice had increased circulating platelet factor 4 expression (**Figure 1D**)

127 and increased platelet reactivity compared to their baseline pre-tumor state (**Figure 1E, F**), with no difference in
128 spontaneous or thrombin induced platelet reactivity between male and female mice (**Figure S2G-J**). Likewise,
129 across patients with GBM, Using Mendelian randomization analyses, we found PAR4 expression is predictive of
130 GBM diagnosis, whereas other platelet receptor expression was not predictive (**Figure S3A-C**). This observation
131 is consistent with previous reports indicating that agonist-induced platelet activation and spontaneous platelet
132 activation were both increased in patients with late-stage metastatic cancer[21] and further suggest that tumor-
133 induced platelet reactivity is mediated by PAR4.
134
135 **Inhibiting platelets via the thrombin-PAR4 signaling axis prolongs survival in a sex-dependent manner**
136
137 To investigate the role of platelets in GBM tumor progression, we intracranially transplanted C57BL/6 mice with
138 murine GBM cells followed by subsequent depletion of platelets through intravenous administration of anti-
139 glycoprotein 1b (GP1b) antibody and survival analysis. These proof-of-concept studies demonstrated that
140 platelet depletion prolongs survival in female tumor-bearing mice (**Figure 2A, Figure S4A**). Depletion of platelets
141 had no effect in male mice in both tumor models (**Figure 2B, Figure S4B**), despite similar levels of platelet
142 depletion between male and female mice (**Figure 2C, Figure S4C**). These results, in combination with the
143 positive correlation between platelet expression and intratumoral immunosuppressive immune cell populations
144 (**Figure 1A**), suggest that platelets drive tumor growth in a sex-biased manner, prompting us to question whether
145 inhibiting the enhanced PAR4-mediated platelet reactivity may also show a sex difference in survival benefit.
146
147 We transplanted C57BL/6 mice with murine GBM cells and pharmacologically targeted the major platelet PAR
148 receptor in mice (PAR4) with daily oral gavage treatment with the PAR4 antagonist BMS986120. Inhibiting PAR4
149 in tumor-bearing mice prolonged survival in a sex-dependent manner, with marked survival in females and no
150 impact in males in all three murine GBM models tested (**Figure 2D-G**, **Figure S5A-B**). We further confirmed this
151 sex-specific survival advantage using dabigatran, a direct inhibitor of thrombin, the PAR4 ligand (**Figure S5C-**
152 **D**). To determine whether these effects were due to higher PAR4 expression in females, we examined
153 intratumoral PAR4 (F2RL3) expression in GBM patient samples (TCGA) and found no difference in expression
154 between tumors from males and those from females (**Figure S5E**). Subsequently, we measured surface and

155 total PAR4 expression on mouse platelets and also found no difference in expression between males and
156 females (**Figure S5F-G**). These studies suggest that inhibiting platelets via PAR4 results in prolonged survival
157 in a sex-dependent manner.
158
159 To ascertain whether the effects observed were specific to PAR4 and not an off-target effect of BMS986120, we
160 transplanted tumor cells into PAR4-P322L, which have a 70% reduction in PAR4 function[22], and PAR4-/-
161 transgenic animals. Consistently, we observed that female PAR4-P322L mice had a longer survival when
162 compared to wildtype animals, whereas we observed no difference in male PAR4-P322L mice (**Figure 2H-I**).
163 This was further confirmed in the PAR4-/- model, where female PAR4-/- mice had a longer survival compared to
164 wildtype female animals, with no difference in male PAR4-/- mice (**Figure 2J-K**).
165
166 **Inhibiting the thrombin-PAR4 signaling axis prolongs survival in a female estrogen dependent manner**
167
168 To investigate the impact of sex chromosomes, sex hormones, and their interaction on the female survival
169 advantage when the thrombin-PAR4 signaling axis is targeted, we utilized the four-core genotype mouse model,
170 which separates the effects of sex chromosomes from gonadal hormones. Using this model, we observed that
171 chromosomal male (XY)-hormonal female mice exhibit a BMS986120-mediated survival advantage similar to
172 that of wildtype females (**Figure 3A-B**), whereas chromosomal female (XX)-hormonal male mice do not (**Figure**
173 **3C-D**). These results suggest that the survival advantage seen upon BMS986120 administration is dependent
174 on female sex hormones. To further validate this hormone dependency, we performed ovariectomies on female
175 mice. One month later, we intracranially implanted GBM cells and administered BMS986120. Estrogen depletion
176 rescued any prior survival benefit observed with BMS986120 administration compared to sham-operation control
177 mice (**Figure 3E**). Finally, to determine whether this was estrogen specific, we utilized estrogen receptor-β
178 knockout (ERβ$^{-/-}$) mice to determine whether the female-specific survival benefit persisted in the absence of
179 ERβ. Strikingly, genetic deletion of ERβ completely abolished the enhanced survival response to BMS986120 in
180 female tumor-bearing mice (**Figure 3F**). These findings indicate that the female survival advantage is strictly
181 ERβ-dependent and strongly support a model in which estrogen receptor signaling is required for the sex-specific
182 effect of PAR4 inhibition.

183

184 **Estrogen Receptor-β interacts with PAR4 and regulates PAR4 signaling**

185 To determine whether the estrogen-dependent survival advantage is due to an estrogen response element on
186 the *F2RL3* (PAR4-encoding gene) promoter, we treated pre-platelet megakaryocyte (MEG-01) cells with β-
187 estradiol, dihydrotestosterone, or progesterone and explored *F2RL3* mRNA and PAR4 protein expression. We
188 found that β-estradiol (**Figure S6A-B**), progesterone (**Figure S6C-D**), or dihydrotestosterone (**Figure S6E-F**)
189 had no effect on *F2RL3* mRNA and PAR4 protein expression. This suggests that *F2RL3* mRNA and PAR4 protein
190 expression are not altered by estrogen, progesterone, or androgen treatment, arguing against direct sex
191 hormone regulation of the PAR4 promoter.

192

193 Given that the female-specific survival benefit of PAR4 inhibition was ERβ dependent, we next asked whether
194 ERβ directly influences PAR4. To address this, we examined PAR4 expression and its interaction with ERβ. Our
195 immunofluorescence imaging of MEG-01 cells revealed co-expression of PAR4 and Erβ (**Figure 4A**), suggesting
196 these two receptors may physically interact. Indeed, lysates immunoprecipitated with ERβ and probed for PAR4
197 (**Figure 4B**) or the reciprocal (**Figure 4C**) revealed these proteins are in complex. This interaction was further
198 confirmed by ERβ immunoprecipitation in human female platelets (**Figure 4D**) and human female brain
199 microvascular endothelial cells (**Figure 4E**). These results suggest Erβ physically associates with PAR4 in
200 platelets and endothelial cells, supporting a direct molecular interaction that may underlie the estrogen-
201 dependent modulation of PAR4 signaling.

202

203 Next, we evaluated PAR4 signaling and its inhibition by BMS986120 in the presence of β-estradiol to determine
204 whether estrogen induces estrogen receptor-dependent regulation of PAR4. Knowing that calcium signaling is
205 downstream of PAR4, we evaluated calcium. Using Fura-2 calcium imaging, we confirmed that PAR4 inhibition
206 with BMS986120 suppresses Ca^{2+} signaling in MEG-01 cells, even when exposed to dihydrotestosterone
207 (**Figure 4F**) or progesterone (**Figure S6G**). However, BMS986120 inhibition of PAR4 signaling was rescued
208 when β-estradiol is present (**Figure 4G**). Additionally, utilizing a G-protein couple receptor (GPCR) phospho-
209 array, we found that estrogen uniquely promotes coordinated activation of calcium-enriched signaling pathways
210 in MEG-01 cells, a response not observed with testosterone. Estrogen engaged ERβ-dependent signaling

211 marked by increased phosphorylation of SRC and PYK2, in addition to modulation of MAPK and PI3K signaling
212 components (**Figure 4H-L**), recapitulating the established ERβ–SRC–PYK2–PI3K platelet signaling axis and
213 overlapping with PAR4-dependent calcium regulation. Estrogen exposure induced coherent activation of
214 calcium-responsive kinases, including CAMK2β/γ/δ and CAMK4, preservation of integrin-associated proteins,
215 and selective activation of PKC isoforms (**Figure 4H-L**), consistent with sustained intracellular Ca^{2+} flux. These
216 upstream events converged on Ca^{2+}-linked MAPK intermediates, reflected by increased RSK and MSK
217 phosphorylation, indicating engagement of the canonical CAMK-MAPK cascade. Together, these findings
218 indicate that estrogen uniquely drives a calcium-dominant GPCR signaling program in megakaryocytes.
219
220 **Inhibiting thrombin-PAR4 signaling enhances CD8+ T cells in a sex-dependent manner**
221
222 Next, we sought to determine the mechanism by which inhibiting the thrombin-PAR4 signaling axis prolongs
223 survival in a sex-dependent manner. To determine whether the effect of BMS986120 was tumor cell intrinsic, we
224 assessed proliferation in multiple murine GBM cell models treated with BMS986120 and observed no major
225 differences in proliferation *in vitro* (**Figure S7A-B**), suggesting no significant impact on tumor cell fitness with
226 BMS986120 treatment. These results led us to test whether the survival benefit seen in female tumor-bearing
227 mice requires a fully functioning immune system. We intracranially transplanted NOD *scid* gamma (NSG) mice
228 with murine GBM cells and subsequently inhibited PAR4 with BMS986120 administration. Pharmacologically
229 inhibiting PAR4 with BMS986120 in immunodeficient mice did not show the survival benefit observed in immune-
230 competent models (**Figure 5A, Figure S7C-D**). These findings reveal that the survival advantage observed in
231 females when inhibiting the thrombin-PAR4 signaling axis depends on a functional immune system.
232
233 Platelets are known to influence immune cell function within the TME and in the systemic circulation[23-27]. While
234 heterologous cell interactions are known to impact GBM, the question of whether platelets have sex-dependent
235 effects is unexplored, and no studies have examined how PAR4 signaling regulates the TME across
236 malignancies. To determine how the thrombin-PAR4 signaling axis contributes to the TME, we conducted
237 immune profiling on tumor-infiltrating immune cells. We found that BMS986120-treated female mice had an
238 increased percentage of CD45hi/CD3+ cells, specifically CD45hi/CD8+ tumor-infiltrating T cells 14 days post

239 tumor implantation (**Figure 5B, Figure S7E, Table S5**), with no changes in other T cell populations or exhaustion
240 markers (**Figure S8**). This BMS986120-mediated increase in CD8+ T cells was also seen at 10 days post
241 BMS986120 treatment (**Figure S9, Table S5**), but not at day 7 (**Figure S10, Table S5**). Consistently,
242 BMS986120-treated female CD8+ T cells had an increase in cytokine expression upon *ex vivo* stimulation at day
243 14 (**Figure 5C Table S6**) but not day 10 or day 7 (**Figure S9C-E**, **Figure S10C-E, Table S6**). There were no
244 differences in other TME immune cell subsets (**Figure S11A-E, Figure S12A-H, Figure S13, Figure S14, Table**
245 **S7**).
246
247 To further validate that the female survival benefit was CD8+ T cell dependent, we intracranially transplanted
248 GBM cells into *Rag1-/-* mice, which lack T and B cells, and treated with BMS986120. Removing T cells reversed
249 the survival benefit observed when mice were treated with BMS986120 (**Figure 5D**); however, when regulatory
250 T cells (Tregs) were removed by treating tumor-bearing *FoxP3-DTR* mice with BMS986120, female mice still
251 exhibited a survival advantage (**Figure S15**). To further isolate the effect specifically to CD8+ T cells, we
252 intracranially implanted murine GBM cells into C57BL/6 mice and administered anti-CD8 depletion antibody in
253 combination with BMS986120. Depletion of CD8+ T cells in the presence of BMS986120 completely rescued
254 the female survival benefit observed when the thrombin-PAR 4 signaling axis was targeted (**Figure 5E, Figure**
255 **S15B**). Lastly, using Akoya multiplex immunofluorescence imaging, we demonstrated that BMS986120 results
256 in a decrease in intratumoral platelet expression (**Figure 6A-H, Figure S16A-D**) and an increase in CD8+ T cell
257 expression in females, with no change in intratumor platelet or CD8+ T cell expression observed in male
258 BMS986120 treated mice (**Figure 6I-N**). Distance proximity analysis between platelets and CD8+ T cells
259 demonstrate trends where BMS986120 decreases the number of platelets in proximity to CD8+ T cells in both
260 males and females (**Figure S16E**). Taken together, our results suggest that the survival benefit of inhibiting
261 thrombin-PAR4 signaling in GBM is sex dependent, driven by sex hormones, and mediated through a decrease
262 in platelet interactions with CD8+ T cells in the TME, highlighting a unique platelet-immune mechanism
263 underlying therapeutic outcome.
264
265 **Inhibiting PAR4 enhances platelet secretion and Ca^{2+} signaling in an estrogen-dependent manner**
266

267 PAR receptors, including PAR4, are thought to be expressed on platelets, endothelial cells and T cells[28],
268 implicating two potential mechanisms that could occur when PAR4 is targeted: a direct enhancement of CD8+ T
269 cells in females or the inhibition of PAR4 signaling on platelets, which then indirectly enhances CD8+ T cell
270 activity in females. To this end, we explored PAR expression in human and mouse T cells by utilizing publicly
271 available datasets. We found that PAR4 was not expressed on T cells from mice (**Figure S17A-D)** or human
272 (**Figure S18A-D)**. However, mice (**Figure S17A-D)** and human (**Figure S18A-D**) T cells did express high levels
273 of PAR1. These results suggest that the increased tumor-infiltrating CD8+ T cells observed when inhibiting PAR4
274 in females is platelet dependent and that platelet signaling likely regulates tumor-infiltrating CD8+ T cells in a
275 sex-dependent manner via PAR4.
276
277 We next determined the impact of pharmacologically inhibiting platelet PAR4 signaling on platelet function and
278 signaling in tumor-bearing mice. We initially isolated platelets from male and female control and tumor-bearing
279 mice and treated them with BMS986120 *ex vivo*. Using flow cytometry, we found no differences in p-selectin and
280 activated GPIIb/IIIa (JON/A) between tumor-bearing male and female platelets *ex vivo* (**Figure S19A, B**). These
281 findings indicate that acute, *ex vivo* pharmacologic inhibition of PAR4 does not intrinsically alter platelet activation
282 or α-granule secretion in a sex-dependent manner, suggesting that the sex-specific effects of PAR4 inhibiting
283 observed in vivo likely require the tumor microenvironment or sustained systemic signaling rather than direct
284 platelet-intrinsic differences alone. Next, we intracranially transplanted GBM cells and treated mice with
285 BMS986120 for 14 days. Aggregation assays demonstrated that pharmacologically inhibiting PAR4 for 14 days
286 had no effect on aggregation/thrombosis in tumor-bearing mice (**Figure 7A**). However, flow cytometry for p-
287 selectin on platelets showed that female tumor-bearing mice had inhibited α-granule secretion following a 14-
288 day treatment with BMS986120 (**Figure 7B, Figure S19C**), whereas male mice treated with BMS986120 had
289 no change in alpha granule secretion (**Figure 7C, Figure S19D**).
290
291 Proteomic GO enrichment analysis demonstrated that peripheral platelets from BMS986120-treated female mice
292 had enriched platelet degranulation and exocytosis signaling pathways (**Figure 7D**). Additionally, the most highly
293 enriched pathway in BMS986120-treated female mice was elevated platelet cytosolic Ca^{2+}. Consistently, GO
294 enrichment analysis on vehicle-treated male and female tumor-bearing mice showed differences in several

295 transport and exocytosis pathways, with no difference in elevated platelet cytosolic Ca^{2+} between male and
296 female untreated platelets (**Figure S19E**).
297
298 Calcium is essential for $CD8^+$ T-cell activation, promoting their recruitment, cytokine production, and cytotoxic
299 function through Ca^{2+}-dependent signaling pathways[29]. To address whether the enhanced Ca^{2+} signaling in
300 female platelets when inhibiting PAR4 with BMS986120 is responsible for increased CD8+ T cell function in the
301 TME, we pre-treated platelets with the calcium release-activated calcium (CRAC) channel blocker YM-58483 or
302 the calcium ionophore ionomycin. We found that pre-treating platelets with YM-58483, inhibited cytokine
303 expression similar to that of platelets; however, pre-treating platelets with ionomycin enhanced cytokine
304 expression in CD8+ T cells (**Figure 7E-H**), with a more pronounced effect in females (**Figure 7E-F**) than in males
305 (**Figure 7G-H**). Together, these results suggest that PAR4 inhibition enhances tumor-infiltrating $CD8^+$ T cells
306 through a platelet-intrinsic, sex-dependent mechanism in which pharmacologic inhibition of PAR4 selectively
307 alters calcium signaling and α-granule secretion in female platelets without affecting global aggregation.
308
309 **Bidirectional regulation of functions between platelets and CD8+ T cells in GBM**
310
311 Our observations and previous work have demonstrated that high platelet counts associate with poor survival in
312 GBM and multiple other malignancies[4, 30-33]. Platelets also interact with and educate the function of other cells,
313 including immune cells that have been identified in the TME and within the circulation[23-27]. However, the role of
314 platelets in regulating the immunosuppressive TME remains poorly understood. When CD8+ T cells were co-
315 cultured with fresh platelets (provided daily), directly or using a transwell, T cell function as measured by
316 intracellular cytokine expression (**Figure 8A-B, Figure S20A-B**) and cytokine secretion (**Figure 8C-D**), was
317 inhibited. When PAR4 function was decreased to 60% by using platelets from PAR4-P322L mice, this observed
318 effect was reversed in females but not male mice (**Figure 8A-B**). Additionally, inhibiting PAR4 with BMS986120
319 reversed the effect of platelets on cytokine secretion in females but not males (**Figure 8C-D**). In an *in vivo* setting,
320 GBM tumor-bearing immunocompetent mice have constitutively higher platelet reactivity relative to their
321 baseline. However, platelet hyperreactivity was not observed in tumor-bearing NSG mice, which lack T, B, and
322 NK cells (**Figure S20C**). To further decipher whether tumor-induced platelet reactivity is T cell specific, GBM

323 tumors were induced in *Rag1-/-* mice, which have no B or T cells. In this case, no increase in platelet reactivity
324 was observed (**Figure 8E**). Consistently, we also tested platelet activity in tumor-bearing mice that were
325 pretreated with an anti-CD8 antibody, and no enhanced platelet reactivity was found (**Figure 8F**). These results
326 reveal that tumor-induced platelet reactivity in murine GBM models is dependent on the presence of immune
327 cells, particularly CD8+ T cells, and that subsequent CD8+ T cell inhibition of platelets is dependent on PAR4
328 (**Figure 8G**).
329

330 **Discussion**

331 Our study identifies a novel connection between platelet signaling, hormonal regulation, and immune activity
332 within the GBM TME. Here, we show that GBM patients exhibit heightened platelet reactivity driven specifically
333 by PAR4 signaling. In murine GBM models, both pharmacological inhibition of PAR4 using BMS986120 and
334 genetic deletion of PAR4 significantly prolonged survival in females but not males. This survival advantage is
335 estrogen dependent: it is preserved in chromosomal male–hormonal female mice within the four-core genotype
336 model and is rescued in ovariectomized mice treated with estrogen. The survival benefit is TME specific and is
337 mediated by platelet-driven enhancement of $CD8^+$ T cell infiltration into the tumor. Inhibition of platelet PAR4
338 signaling increases calcium signaling through an estrogen-dependent interaction between PAR4 and estrogen
339 receptor β (ERβ), a receptor interaction not previously described.

340 Although BMS986120 reduced platelet–$CD8^+$ T cell proximity in both males and females, only females
341 demonstrated a corresponding increase in intratumoral $CD8^+$ T cell accumulation. We speculate that this
342 divergence reflects estrogen–estrogen receptor β signaling in female platelets, which may uniquely couple
343 thrombin–PAR4 inhibition to enhanced $CD8^+$ T cell recruitment and/or retention within the tumor
344 microenvironment. PAR4-activated platelets within the TME suppress $CD8^+$ T cell function, and depletion of
345 $CD8^+$ T cells abolishes both the tumor-induced platelet reactivity and the survival benefit conferred by PAR4
346 inhibition (**Figure 8G**). This is achieved through perturbations in immune function within the TME, leading to
347 sex bias in immune cell subpopulations such as microglia, MDSCs, and T cells[8-10]. This study highlights
348 cancer-associated thrombosis as a key driver of tumor progression, supporting precision medicine strategies
349 that account for sex as a biological variable.

350

351 Cancer patients have a significantly higher risk of developing thrombotic events compared to the general
352 population, with an estimated ninefold increase in venous thromboembolism risk[13, 14, 34, 35]. Recent studies
353 highlight the role of platelet activation in the TME, where they influence immune responses and promote pro-
354 thrombotic conditions[7]. One likely source of thrombin in the GBM TME is the tumor cells themselves: we
355 previously showed that cancer stem cells (CSCs) can endogenously produce all coagulation cascade
356 components and generate biologically active thrombin locally — independent of plasma — providing a direct
357 source within the tumor. In addition, thrombin in the TME could arise from: (1) expression of procoagulant factors
358 (e.g., tissue factor) by tumor or stromal cells that drive local coagulation [16, 36, 37] ; (2) disturbed or leaky tumor-
359 associated vasculature, leading to plasma protein extravasation and local activation of coagulation; or (3) pro-
360 coagulant extracellular vesicles or microparticles released by tumor, endothelial, or immune cells that catalyze
361 thrombin generation. The broader phenomenon of tumor-driven coagulation activation via tissue factor and
362 coagulation cascade components has been well described in solid cancers (and brain tumors).

363 Our work expands on this concept by demonstrating that tumor formation heightens platelet reactivity through
364 an additional platelet receptor, PAR4, which directly contributes to immune suppression in a sex-dependent
365 manner. This underscores how tumors hijack normal physiological processes to create a microenvironment that
366 supports their progression and survival. Our findings emphasize the importance of inhibiting cancer-associated
367 thrombosis and platelet activation and suggest that, with further study, selective anticoagulation strategies might
368 complement existing therapies and potentially enhance antitumor responses. Additionally, although this study
369 focuses on GBM, the mechanistic coupling among platelet PAR4 signaling, thrombotic pathways, and immune
370 modulation suggests broader relevance across cancers with high thrombotic burden. In addition to triple-negative
371 breast cancer, these pathways may be particularly relevant in estrogen receptor-positive malignancies, where
372 estrogen signaling could further intersect with platelet activation and immune regulation. Together, these
373 observations raise the possibility that sex- and hormone-dependent PAR4 signaling may influence antitumor
374 immunity across multiple cancer types, including pancreatic, colon, and lung cancers, warranting future
375 investigation.

376

377 Inhibiting PAR4 offers a therapeutic advantage over inhibiting PAR1 due to its distinct signaling kinetics, which
378 reduce bleeding risks while still effectively modulating platelet activity[22, 38, 39]. Unlike PAR1, which responds

379 rapidly to low thrombin concentrations, PAR4 requires higher thrombin levels for activation, leading to more
380 highly controlled platelet responses and minimizing excessive bleeding complications. Additionally, PAR4
381 mediates the prolonged signaling necessary for stable thrombus formation, whereas PAR1 activation results in
382 a rapid, transient signal. By selectively inhibiting PAR4, therapeutic strategies can limit thrombosis while
383 preserving essential hemostatic functions, reducing the likelihood of severe bleeding events associated with
384 PAR1 inhibition[22]. Previous work has demonstrated that inhibiting PAR4 enhances CD4+ T regulatory cells,
385 contributing to immunosuppression[40]; however, our results show that PAR4 inhibition enhances CD8+ T cell
386 function in a sex-dependent manner. This could be because T cells in brain tumors often exhibit exhaustion,
387 immunosuppression, and altered metabolism, which weaken their ability to effectively combat the tumor[41].
388 Compared to other tumor types, T cells in brain tumors face heightened challenges due to the brain's unique
389 immune-privileged status and the suppressive tumor microenvironment, which includes factors like regulatory T
390 cells and tumor-associated macrophages[42]. These elements contribute to reduced T cell infiltration and impaired
391 antitumor responses. These findings highlight PAR4 as a more favorable target for platelet inhibition in cancer-
392 associated thrombosis and other thrombotic disorders in females.

393

394 While our findings establish the role of PAR4-mediated platelet signaling in GBM progression and its sex-
395 dependent therapeutic implications, several limitations remain. Translating results from murine models to human
396 patients requires further clinical validation across diverse genetic and tumor backgrounds. Additionally, while
397 estrogen contributes to the survival benefit of PAR4 inhibition, broader hormonal influences on platelet function
398 and immune modulation warrant further exploration. An important consideration not addressed in the present
399 study is the impact of cyclical estrogen fluctuations on PAR4 expression and therapeutic response. Although
400 hormone cycle-dependent regulation of PAR4 could have implications for optimizing the timing of PAR4
401 antagonist administration, incorporating estrous cycle–specific analyses in an intracranial GBM model presents
402 substantial technical and logistical challenges, including longitudinal hormone monitoring and repeated tissue
403 sampling. Future studies specifically designed to integrate hormone-cycle staging with PAR4 expression and
404 drug timing will be critical to determine whether estrogen-dependent dynamics can be leveraged to inform
405 personalized dosing strategies for PAR4-targeted therapies. Additionally, the therapeutic potential of BMS986120

is promising, but the long-term efficacy, safety, and off-target effects must be assessed in preclinical and clinical models.

Based on our findings, future research is well positioned to investigate alternative platelet secretion mechanisms in shaping immune responses, with proteomic analyses identifying sex-specific signaling pathways that influence treatment efficacy. Examining how estrogen affects platelet-driven TME dynamics may yield novel hormone-modulating strategies to complement PAR4-targeted therapies. Expanding these insights into human studies and developing biomarkers for platelet activity could better predict patient outcomes. Our findings highlight the importance of addressing cancer-associated thrombosis and platelet activation as potential therapeutic targets and suggest that future studies should explore how anticoagulation strategies might interact with immune processes in GBM to improve patient outcomes.

417 **Materials and Methods**

418

419 *Cell models*

420

421 The syngeneic mouse GBM cell line SB28 was generously gifted by Dr. Hideho Okada (University of California
422 San Francisco), and KR158 was generously gifted by Dr. Loic P. Deleyrolle (Mayo Clinic, previously University
423 of Florida). The GL261 line was from the Developmental Therapeutics Program, NCI. MEG-01 cells were
424 generously gifted by Dr. Scott J. Cameron (Cleveland Clinic Research). All cell lines were routinely tested for
425 *Mycoplasma* and were preemptively treated with 1:100 MycoRemoval Agent (MP Biomedicals) upon thawing.
426 All cell lines used in these studies were maintained in complete RPMI 1640 (Media Preparation Core, Cleveland
427 Clinic Research) supplemented with 10% FBS (Thermo Fisher Scientific), 1% penicillin/streptomycin (Media
428 Preparation Core, Cleveland Clinic Research). All cell lines were maintained at 37°C and 5% CO_2 in a humidified
429 incubator.

430

431 *Mice*

432

433 All animal experiments were performed in accordance with Cleveland Clinic IACUC policies and guidelines and
434 approved by the IACUC committee at Cleveland Clinic Research. C57BL/6 (RRID:IMSR_JAX:0006641), *Rag1*$^{-}$
435 $^{/-}$ (B6.129S7-*Rag1*^{tm1Mom}*/J*; RRID:IMSR_JAX:002216), four-core genotye (FCG) (B6.Cg-
436 Tg(Sry)2Ei *Sry*^{dl1Rlb}/JtuJ), and NOD.Cg-*Prkdc*^{scid} *Il2rg*^{tm1Wjl}/SzJ (NSG; RRID:IMSR_JAX:005557) mice were
437 purchased from The Jackson Laboratory as required. PAR4-P322L and PAR4-/- mice were a generous gift from
438 Dr. Marvin Nieman at Case Western Reserve University[22]. Estrogen receptor beta knockout (Erβ-/-) mice were
439 a generous gift from Dr. Wendy Goodman at Case Western Reserve University.

440

441 *Intracranial tumor transplantation and treatments*

442

443 For intracranial tumor implantation, 4- to 7-week-old mice were intracranially injected with 10,000 to 20,000 cells
444 in 10 µL of RPMI-null media, 3 mm caudal to the coronal structure, 1.8 mm lateral to the sagittal suture at a 90°

445 angle with the skull to a depth of 3.0 mm. Animals were monitored daily for neurological symptoms that include
446 lethargy and hunched posture to qualify signs of tumor burden. In some experiments, male and female mice
447 were treated with 2 mg/kg BMS986120 (MedChemExpress) or vehicle (8% DMSO) via oral gavage, daily,
448 beginning 1-7 days post tumor implantation depending on the tumor latency of the model. In other experiments,
449 to deplete CD8+ T cells, mice were intraperitoneally injected with an anti-CD8 antibody (BioXCell, Cat. #0061)
450 or isotype control antibody (BioXCell, cat. #BE0090). Animals were administered 200 µg of antibody on day -1,
451 followed by 100 µg every 5 days until humane endpoint was reached as previously described[10]. In other
452 experiments, to deplete platelets, anti-GPIbα (EMFRET, Cat. R300) or anti-igG was administered
453 intraperitoneally 1 day post tumor implantation to avoid hemorrhage at a concentration of 1 µg/g. Subsequent
454 administration was performed at a concentration of 0.5 µg/g every 5 days until humane endpoint was reached.
455
456 *Ovariectomy*
457
458 For oophorectomy procedures, 4- to 7-week-old female mice were deeply anesthetized, and a longitudinal
459 incision was made 0.5 cm above where the upper border line of the two hind limbs connect with the back. The
460 skin incision was pulled approximately 0.5 cm horizontally to the left or the right to visualize two soft, white, shiny
461 fat masses next to the lower pole of the kidneys. The left and right ovaries of the mouse are found in the
462 respective fat masses and were bi-laterally ovariectomized by cutting each side of the ovary and excising with
463 sterile surgical scissors, which results in little to no bleeding. After the muscle layer was closed with sutures and
464 the skin incision was sutured or stapled, the mice were placed in a heated chamber to recover. Mice in the sham
465 group also underwent a similar procedure as the ovariectomized group, except the ovaries were left intact and
466 only some adipose tissue near the ovaries was removed.
467
468 *Human platelet isolation and stimulation*
469
470 Human platelet isolation was conducted as previously described[43, 44]. In brief, whole blood was collected from
471 healthy donors into tubes containing 3.2% sodium citrate (BD Vacutainer) using a 21-gauge butterfly needle to
472 ensure minimal activation during collection. Platelet-rich plasma (PRP) was obtained by centrifuging the collected

473 blood at 200 x g for 15 minutes at room temperature, carefully avoiding the buffy coat. PRP was then subjected
474 to a second centrifugation at 200 x g for 15 minutes to further purify the sample. The resulting supernatant was
475 discarded, and the PRP was diluted 1:1 with Tyrodes buffer. Prostaglandin I2 (PGI2, 10 nM final concentration)
476 was added to prevent spontaneous platelet activation during the isolation process. The PRP-Tyrode's mixture
477 was centrifuged at 1,400 x g for 5 minutes to pellet the platelets, and the supernatant was removed. Washed
478 platelets were resuspended in Tyrode's buffer and diluted 1:10 to achieve a working platelet suspension. Fifty
479 million platelets per mL was used immediately for subsequent activation assays.

480 For platelet activation, aliquots of 100 µL of the platelet suspension were stimulated with increasing
481 concentrations of agonists inhibiting the PAR1 receptor (TRAP6), the thromboxane receptor (U46619), the
482 P2Y12 receptor (ADP), and PAR4 (AY-NH2). Agonist concentrations ranged from 0.01 µM to 20 µM for TRAP6,
483 U46619, and ADP, and from 0.05 µg/mL to 1 µg/mL for CRP. After a 15-minute stimulation at room temperature,
484 1 µL of P-selectin antibody (anti-CD62P, clone AK-4, eBioscience) conjugated to PE was added to each sample
485 and incubated in the dark for 30 minutes to prevent photobleaching.
486
487 Following antibody staining, 100 µL of 2% formalin was added to each sample to fix the platelets. Fixed samples
488 were stored at 4°C for no longer than 16 hours prior to analysis. Flow cytometry was performed on a BD Accuri
489 C6, and fluorescence was detected using the FL-2 channel (for PE-conjugated antibodies). Platelet activation
490 was quantified based on the surface expression of CD62P, with data analyzed using FlowJo software.
491
492 *Mouse platelet isolation and stimulation*
493
494 Whole blood was collected from C57BL/6 mice via retro-orbital bleeding using heparinized capillary tubes. Blood
495 was drawn into tubes containing heparin/Tyrode's solution (1000 U/mL heparin in Tyrode's buffer, 1:20 dilution).
496 The collected blood was gently mixed by inverting the tube and processed immediately. PRP was isolated by
497 centrifuging the whole blood at 1000 RPM for 5 minutes at room temperature. Plasma was carefully collected,
498 avoiding red blood cells, and subjected to a second centrifugation at 1000 RPM for 5 minutes to remove
499 remaining blood cells. The PRP was then supplemented with 1 µM PGI2 to prevent platelet activation during
500 isolation. The platelet pellet was obtained by centrifuging PRP at 2700 RPM for 5 minutes, after which the

501 supernatant was discarded. Platelets were resuspended in Tyrode's buffer and pooled to achieve a final
502 concentration suitable for stimulation experiments. Platelets were aliquoted into 96-well plates at a concentration
503 of 100 μL per well for subsequent activation assays.
504 For platelet activation, 1 μL of each agonist (thrombin, U46619, ADP, convulxin) was added to the platelets, with
505 final concentrations ranging from 0.1 to 20 μM, depending on the agonist. Platelet stimulation was carried out at
506 room temperature for 10 minutes. After stimulation, 1 μL of FITC-conjugated anti-CD62P antibody (clone
507 RB40.34, BD Biosciences) was added to each sample, and the platelets were incubated in the dark for an
508 additional 10 minutes to prevent photobleaching.
509
510 Following staining, 100 μL of 2% formalin was added to fix the platelets, and samples were either immediately
511 analyzed by flow cytometry or stored at 4°C for up to 16 hours prior to analysis. Flow cytometry was performed
512 on a BD Accuri C6 cytometer, and data were collected for 10,000 events per sample. The expression of P-
513 selectin (CD62P) on the platelet surface was used as an indicator of platelet activation, and data analysis was
514 carried out using FlowJo software.
515
516 *Immunophenotyping by flow cytometry*
517
518 At the designated time points, tumor-bearing left hemispheres were enzymatically digested using collagenase
519 IV (Sigma) and DNase I (Sigma) to generate a single-cell suspension, subjected to a Percoll centrifugation step,
520 and then filtered through a 40-μm strainer. Cells were first stained with LIVE/DEAD Fixable Stains (Thermo
521 Fisher) on ice for 15 minutes, washed with PBS, and resuspended in an Fc receptor blocker (Miltenyi Biotec)
522 diluted in PBS/2% BSA, followed by incubation on ice for 10 minutes. Surface staining was performed using
523 fluorochrome-conjugated antibodies diluted in brilliant buffer (BD Biosciences) at a concentration of 1:100 to
524 1:250, with a 30-minute incubation on ice. After a subsequent wash in PBS/2% BSA, cells were fixed overnight
525 using Foxp3/Transcription Factor Fixation Buffer (eBioscience).
526
527 For intracellular staining, antibodies were prepared in Foxp3/Transcription Factor Permeabilization Buffer at
528 1:250 to 1:500 and incubated at room temperature for 45 minutes. To detect intracellular cytokines, cells were

529 stimulated in complete RPMI medium using a Cell Stimulation Cocktail with a protein transport inhibitor
530 (eBioscience) for 4 hours. Following stimulation, cells underwent the same staining procedures as described
531 above.
532
533 *In vitro CD8+ T cell culture*
534
535 CD8+ T cells were extracted from the splenocytes of C57BL/6 mice using a magnetic bead isolation kit
536 (STEMCELL Technologies), following established protocols. The cells were then maintained in complete RPMI
537 medium supplemented with recombinant human IL-2 (30 U/mL, PeproTech) and activated using anti-CD3/anti-
538 CD28 Dynabeads (Invitrogen) at a bead-to-cell ratio of 1:10. In addition, platelets were isolated as previously
539 described and incorporated into the T cell culture for three consecutive days at a 1:1 ratio of CD8+ T cells to
540 platelets. Cells subsequently underwent the same staining procedures outlined above.
541
542 *MEG-01 Cell Culture Experiments*
543
544 MEG-01 cells were cultured in RPMI compete media as described above and treated with β-estradiol (0, 0.01,
545 0.1, 1.0, and 10 μg/ml), dihydrotestosterone (0, 0.01, 0.1, 1.0, and 10 μg/ml), and progesterone (0, 0.01, 0.1,
546 1.0, and 10 μg/ml) for 4 consecutive days for quantitative real time PCR (QPCR), immunoblotting and GPCR
547 phospho antibody array (Full Moon Biosystems).
548
549 *Immunoblotting, Antibodies, and GPCR Phospho antibody array*

550 Lysates were prepared as previousl described by our group[4, 45]. Cells were washed with PBS and lysed in NP-
551 40 lysis buffer (0.5% NP-40, 10 mM Tris-Cl pH 7.5, 1 mM EDTA pH 8.0, 150 mM NaCl) supplemented with 1%
552 protease and phosphatase inhibitors (Sigma-Aldrich). Lysates were clarified by centrifugation at 21,000 × g for
553 10 min at 4 °C, and protein concentration was determined using the Bio-Rad protein assay with BSA as the
554 standard.

555 For immunoblotting, equal amounts of protein (15–50 μg) were resolved by SDS-PAGE on pre-cast 4–15% gels
556 (Bio-Rad) and transferred to PVDF membranes (Millipore). The membrane was subsequently rinsed in Tris-

557 buffered saline (TBS; 50 mM Tris-HCl 150 mM NaCl, pH 7.6) and blocked in Intercept blocking buffer for one
558 hour (Li-Cor, 927-50000, Lincoln, NE) prior to the application of primary antibodies targeting Actin (1:1000)
559 (Millipore Sigma, MAB1501PAR4, PAR4 (1:500) (Generated by Marvin Neiemen)[46], SRC(Tyr418) (1:1000)
560 (ThermoFisher, 14-9034-82), SRC (1:1000) (Cell Signaling 2108), P-PYK2(Tyr881) (1:1000) (ThermoFisher, 44-
561 620G), and PYK2 (1:1000) (ABCAM, ab32571). The membrane was incubated overnight at 4°C with the primary
562 antibody, rinsed with TBS-T (TBS; 50 mM Tris-HCl 150 mM NaCl, 1 % Tween-20 v/v% pH 7.6) followed by
563 incubation in secondary (IRDye 680- and IRDye 800CW-conjugated secondary antibodies, Li-Cor, 926-68072
564 and 926-32213, respectively) for one hour at room temperature prior to visualization on the Li-Cor Odyssey CLx
565 imaging System (Li-Cor, Lincoln, NE). Western blot analysis of band intensity was completed using Image Studio
566 Analysis software from Li-Cor. Alternatively, Membranes were incubated with primary antibodies in 5% BSA in
567 TBST at 4 °C for 2–7 days, washed with TBST, and then incubated with HRP-conjugated secondary antibodies
568 for 2.5–3 h at room temperature. Blots were developed using enhanced chemiluminescence (ECL) and imaged
569 on a Bio-Rad ChemiDoc MP system. Actin was used as a loading control.

570 For the GPCR Phospho antibody array (Full Moon Biosystems, PGP193) was conducted following the protocol
571 as described by the company. Following array incubation in antibody, slides were sent to Full Moon Biosystems
572 for analysis and array signal intensity was quantified as the median signal per spot and averaged across replicate
573 spots for each antibody, with variability assessed by coefficient of variation. Data were normalized to the median
574 signal intensity across the array. Fold changes were calculated as the ratio of treatment to control from
575 normalized values, with increased or decreased expression indicated by red or green shading, respectively. For
576 phospho-arrays, signaling ratios were calculated as the phospho-specific signal divided by the corresponding
577 total protein signal, and fold changes were similarly determined between treatment and control samples.

578 *Co-immunoprecipitation*

579 Co-Ips were done as previously described[47]. Briefly, Cells were lysed on ice for 2 h in 1.0 mL immunoprecipitation
580 (IP) buffer containing 25 mM Tris (pH 7.4), 1 mM $MgCl_2$, 2 mM EDTA, 150 mM NaCl, 1.0% Triton X-100, and
581 Complete Protease Inhibitor Cocktail (Roche). Protein G–Sepharose Fast Flow beads (100 µL; MilliporeSigma)
582 were washed twice with IP buffer (500 × g, 5 min), blocked for 1 h in 5.0% BSA prepared in IP buffer, and
583 resuspended in 1.0 mL IP buffer. Lysates were clarified by centrifugation (12,000 × g, 10 min, 4°C), and 10% of

584 the supernatant (50 μL) was retained as the input control. The remaining lysate was split into two equal aliquots
585 and incubated overnight at 4°C with Protein G beads and either 2 μg of the indicated primary antibody or an
586 isotype-matched IgG control. Following incubation, samples were centrifuged at 500 × g for 5 min, and 50 μL of
587 the supernatant was collected as the unbound fraction. Beads were washed four times with IP wash buffer (25
588 mM Tris [pH 7.4], 10 mM $MgCl_2$, 2 mM EDTA, 0.1% Triton X-100), with 50 μL aliquots retained after the first and
589 fourth washes. After the final wash, bound proteins were eluted by denaturation in 2× SDS sample buffer and
590 heating at 95°C for 10 min. Samples were resolved by SDS-PAGE and transferred to nitrocellulose membranes
591 as described above.

592 *Quantitative real time PCR (qPCR)*

593 MEG-01 cell were incubated at *37 °C in a humidified incubator with 5% CO_2, then rinsed with HBSS. RNA was*
594 *isolated using the RNeasy Mini Kit, quantified for quality and concentration, and reverse-transcribed to cDNA.*
595 *Quantitative PCR was performed using SYBR Green chemistry on a Bio-Rad CFX Connect system to assess*
596 *expression of GSC, platelet, and coagulation-associated genes. Reactions (20 μL) were run in triplicate for 40*
597 *cycles, and relative expression was calculated using the ΔΔCT method.* Primers used were specific for actin (5'-
598 AGAAAATCTGGCACCACACC-3', 5'-AGAGGCGTACAGGGATAGCA-3') and PAR4 (5'-
599 CCGCTGCTGTATCCTTTGGT -3', 5'-TCCTTGAGTTCTACTGTGGGAC-3').

600

601 *MEG-01 calcium imaging*

602

603 Washed MEG-01 were pre-incubated with BMS986120 (10nM), β-estradiol (0, 0.01, 0.1, 1.0, and 10 μg/ml),
604 dihydrotestosterone (0, 0.01, 0.1, 1.0, and 10 μg/ml), and progesterone (0, 0.01, 0.1, 1.0, and 10 μg/ml).
605 Afterwards, washed MEG-01 were loaded with Fura-2 AM (5 μM, 1 h at 37 °C), pelleted by centrifugation (2700
606 rpm, 5 min) in the presence of 10 μM PgI_2, and resuspended in fresh Tyrode's solution in a 96-well plate.
607 Intracellular calcium flux was measured over 10 min by ratiometric fluorescence (340/380 nm) following
608 automated addition of thrombin (1.0 U/mL) using a FlexStation 3 system. Data are presented as normalized
609 fluorescence changes relative to baseline (F/F_0) as previously described[43].

610 **Analysis of previously published scRNA-seq data**

611

612 *Patient samples and datasets*

613

614 This study utilized WHO grade 4 IDH wildtype GBM samples from four publicly available datasets: The Cancer
615 Genome Atlas (TCGA), Chinese Glioma Genome Atlas (CGGA_325, CGGA_893), and Glioma Longitudinal
616 Analysis (GLASS).

617

618 *Immune Cell Profiling*

619

620 The relative abundance of 22 immune cell subtypes within each tumor sample from each dataset was estimated
621 using CIBERSORTx with default parameters and the LM22 signature gene set. Additionally, a gene signature
622 for platelet expression (REACTOME_RESPONSE_TO_ELEVATED_PLATELET_CYTOSOLIC_CA2, MSigDB)
623 was scored for each sample using single sample gene set enrichment analysis (ssGSEA).

624

625 *Univariate survival analysis*

626

627 To evaluate the prognostic significance of immune cell infiltration, univariate Cox proportional hazards models
628 were constructed for each estimated immune cell population (including the Platelet Sig score) within each
629 dataset. Immune cell proportions and platelet signature score were z-score normalized and centered prior to
630 hazard ratio computation. Immune cell abundance and platelet signature score (platelet_sig) were dichotomized
631 at the median value for each cell type within each respective dataset. The resulting hazard ratios (HRs) for overall
632 survival are presented, with error bars indicating the 95% confidence intervals.

633

634 *Immune cell correlation analysis*

635

636 Spearman correlation coefficients between the estimated abundances of the major immune cell types and
637 platelet gene signature score were computed. Correlation coefficients were computed for each of the major

638 immune cell subtypes (B Cells, dendritic cells (DCs), T cells, NK cells, mast cells, microglia, monocytes, and
639 macrophages) within each dataset (CGGA_325, GLASS, TCGA).
640
641 *PAR4 expression analysis in cell subtypes*
642
643 To investigate the expression profile of the PAR4 gene (also known as *F2RL3*) across different cell populations
644 within the GBM TME, we analyzed single-cell RNA sequencing data from the GBMap dataset. The expression
645 level of PAR4 was assessed for various identified cell subtypes as previously annotated. A dot plot (Seurat v5)
646 was generated to visualize the results.
647
648 *Mendelian randomization analysis*
649
650 The European Ancestry consortium was used for this analysis. Genetic variants (G), typically single-nucleotide
651 polymorphisms (SNPs), serve as instrumental variables (IVs) to assess the causal effect of an exposure (X; e.g.,
652 platelet count) on an outcome (Y; e.g., glioma risk). For the causal inference to be valid, three key assumptions
653 must be satisfied: IV1 (Relevance) — the genetic instruments must be robustly associated with the exposure,
654 typically derived from genome-wide association studies (GWAS); IV2 (Independence) — the genetic instruments
655 must not be associated with confounding variables (U) that jointly influence both the exposure and the outcome;
656 and IV3 (Exclusion Restriction) — the instruments must affect the outcome solely through the exposure and not
657 via any alternative biological pathways. The directed acyclic graph visualizes how genetic variants influence the
658 outcome only via their effect on the exposure, assuming no horizontal pleiotropy or confounding from
659 unmeasured variables.
660
661 *Akoya Multispectral Immunofluorescence*

662 *PhenoCycler-Fusion Slide Preparation*

663 FFPE tissue slides were baked at 60 ºC overnight. Baked slides were deparaffinized with Xylene Substitute
664 solution (Epredia) and rehydrated in a series of gradient ethanol solutions, ranging from 100% to ddH2O. The
665 slides were then placed in a glass Coplin jar containing 1X antigen retrieval buffer (pH 9.0) (Akoya Biosciences),

666 and antigen retrieval was performed with an Instant Pot using the high-pressure setting for 20 minutes. Following
667 antigen retrieval, the slides were cooled in the retrieval buffer to RT and transferred to a transparent slide
668 container with an autofluorescence bleaching solution (4.5% w/v H2O2 and 20mM NaOH in PBS). The container
669 was sandwiched between two LED lamps, and the slides were photobleached for 90 minutes at RT, with fresh
670 bleaching solution replenished once after 45 minutes. Slides were then processed according to the PhenoCycler-
671 Fusion User Guide (PD-000011 Rev S, Akoya Biosciences). Briefly, slides were washed in Hydration Buffer,
672 equilibrated in Staining Buffer, and incubated overnight at 4 ºC with a 47-marker antibody cocktail (Table S8)
673 prepared in Blocking Buffer. The slides were then washed in Staining Buffer, gently fixed with 1.6% formaldehyde,
674 washed in PBS, and incubated in ice-cold methanol for 5 minutes. The slides were then washed in PBS, fixed
675 with Final Fixative Solution for 20 minutes, washed in PBS, and preserved in Storage Buffer at 4 ºC before the
676 PCF run.

677 *PhenoCycler-Fusion Setup and Data Acquisition*

678 The experimental protocol was set up using the PhenoCycler Experiment Designer (Version 2.2.0). A reporter
679 plate containing fluorescently labeled reporters was prepared according to the PhenoCycler-Fusion User Guide
680 (PD-000011 Rev S, Akoya Biosciences). Slides were prepared for the PCF instrument according to the
681 PhenoImager Fusion 2.0 User Guide (PD-000088 Rev G, Akoya Biosciences). Briefly, slides were removed from
682 the Storage Buffer and incubated in PBS for 10 minutes at RT. After incubation, a Flow Cell (Akoya Biosciences)
683 was attached to each sample slide using the Flow Cell Assembly Device (Akoya Biosciences). The slide with the
684 attached Flow Cell (Sample Flow Cell) was equilibrated in 1X PCF buffer for 10 minutes at RT. PhenoCycler-
685 Fusion software (Version 2.4.0) was used to set up the imaging run on the PCF instrument according to the
686 PhenoImager Fusion 2.0 User Guide (PD-000088 Rev G, Akoya Biosciences).

687 Reagents were prepared and loaded into appropriate reservoirs on the instrument, and the prepared reporter
688 plate was loaded into the instrument. A new PhenoCycler run was initiated using the experimental protocol
689 design. A blank flow cell was loaded into the Flow Cell Slide Carrier, and all software prompts during the pre-
690 flight routine were followed. The Sample Flow Cell was loaded into the carrier, and a leak check was performed.
691 Automatic sample detection was performed, followed by scan region selection and imaging initiation. Upon
692 completion, the Sample Flow Cell was placed in the Storage Buffer at 4 ºC. The generated QPTIFF data files

693 were used for downstream image analysis. Analysis of the akoya multispectral immunofluorescence imaging
694 was done as previously described[48].

695 *PhenoCycler-Fusion data analysis*

696 We leveraged InstanSeg[49], an embedding-based deep learning model built for cell segmentation, to identify cell
697 boundaries in each region of interest (ROI) extracted from the highly multiplexed immunofluorescence images
698 generated by the Akoya PhenoCycler Fusion. The resulting segmentation mask and a list of de-multiplexed
699 single-channel images from the panel are input to Nimbus[50], a deep learning model that predicts confidence of
700 marker positivity in each cell. These scores, calculated for each channel and bounded between 0 to 1, replace
701 integrated expression for downstream analyses to combat technical confounders like background staining,
702 autofluorescence, and channel intensity variation.

703 By aggregating Nimbus scores across every high quality ROI into a single AnnData object, we applied
704 FlowSOM[51], an unsupervised clustering algorithm based on self-organizing maps, to group cells by their pattern
705 of protein expression. Using the markers enriched in each of the 18 resulting clusters, as identified by the
706 Wilcoxon rank sum test, we manually annotated cell states. We then appended these annotations to the spatial
707 coordinates of each cell for further analysis.

708 To capture acellular features in each ROI, such as platelets, we employed a deep learning model for single-
709 channel bright spot detection in fluorescence microscopy images called Spotiflow[52]. To efficiently calculate the
710 density and proximity of these features around cells, we applied the cKDTree algorithm from the scipy.spatial
711 library[53]. By aggregating these spatial association metrics for each previously defined cell state and comparing
712 across ROI-specific metadata, we investigated sex-specific and treatment-correlated phenotypes.

713 *Code and data availability*

714

715 All data used for the above analyses are publicly available through the TCGA, CGGA, GLASS, and GBMap
716 datasets, including clinical and cell type metadata. Immune cell signatures are available through CIBERSORTx,
717 and the platelet gene signature is available through MSigDB. All analyses were performed in R version 4.3.0,
718 and all code to reproducibly perform these analyses will be provided on Github.

719

720 *Statistical analysis*

721

722 Data visualization and statistical analysis were conducted using GraphPad Prism (Version 9, GraphPad Software
723 Inc., RRID:SCR_002798). Depending on the dataset, unpaired or paired t-tests, as well as one-way or two-way
724 analysis of variance (ANOVA) with multiple comparison adjustments, were applied as described in the figure
725 legends. Survival analysis was evaluated using the log-rank test. For all analysis, statistical significance was set
726 at $p < 0.05$.

727 **Data Availability**

728 All data generated in this study are available upon request from the corresponding author, Dr. Justin D. Lathia
729 (lathiaj@ccf.org).

730

731 **Ethics Declaration**

732 *Competing interests*

733 The authors declare no competing interests.

734

735 **Code availability**

736 All code to reproducibly perform these analyses will be provided on Github. Additionally, all code used in this
737 study are available upon request from the corresponding author, Dr. Justin D. Lathia (lathiaj@ccf.org).

738

739 **Author Contributions**

740 Conception and design: A.R.S, S.J.C, J.D.L

741 Development of methodology: A.R.S, G.B, A.A, J.L

742 Acquisition of data: A.R.S, G.B, D.R, T.J.A, I.J, V.B, L.T, T.N, N.R, S.H, G.P.T, A.V, J.G, X.Y, S.K, J.C, V.S.K,
743 S.S.K, A.S, B. R., N.S., A.D

744 Analysis and interpretation of data: A.R.S, G.B, J. L

745 Writing review: A.R.S, J.L, E.M.H, J.D.R, C.M.O, S.J.C, J.D.L

Administrative, technical, or material support: C.N.H, A.E.S, J.B.R, C.G.H, E.X.S, F.W.L, W.A.G, T.E.M, C.M.O, T.A.C, A.K, M.N., A.D.

Study supervision: S.J.C, J.D.L.

Acknowledgements

We sincerely acknowledge the members of the Lathia laboratory for their valuable insights and constructive discussions and Dr. Reza Khatib for his inspiration and support of our work. We sincerely want to acknowledge Neal Restivo and Oatey Company for their support of our work. We are grateful for the illustrative contributions of Ms. Amanda Mendelsohn from Enterprise Creative at the Cleveland Clinic. We are grateful to Dr. Belinda Willard and her team at the Proteomics Core (Cleveland Clinic Research). Additionally, we extend our gratitude to Drs. Matthew Flick and Silvio Antoniak (University of North Carolina Chapel Hill) for their support and constructive comments on the project. This work was supported by NIH grants NIH T32 CA059366 (A.R.S), F32 CA287655 (A.R.S), R35 NS127083 (J.D.L), P01 CA245705 (J.D.L, J.B.R), HL158801 (SJC), U01HL143402 (AK), and R01HL164516 (A.K.). This work was also supported by the Cleveland Clinic VeloSano Bike to Cure event (S.J.C and J.D.L), Velosano 11 Pilot Grant (S.J.C), and the Midwest Brain Tumor Foundation (A.R.S), Cleveland Clinic (A.K., J.D.L.) and Case Comprehensive Cancer Center (J.D.L.).

References

1. Xiao T, Lee J, Gauntner TD, Velegraki M, Lathia JD, Li Z. Hallmarks of sex bias in immuno-oncology: mechanisms and therapeutic implications. Nat Rev Cancer. 2024;24(5):338-55. Epub 20240408. doi: 10.1038/s41568-024-00680-z. PubMed PMID: 38589557.
2. Ostrom QT, Rubin JB, Lathia JD, Berens ME, Barnholtz-Sloan JS. Females have the survival advantage in glioblastoma. Neuro Oncol. 2018;20(4):576-7. doi: 10.1093/neuonc/noy002. PubMed PMID: 29474647; PMCID: PMC5909625.
3. Aggarwal A, Jennings CL, Manning E, Cameron SJ. Platelets at the Vessel Wall in Non-Thrombotic Disease. Circ Res. 2023;132(6):775-90. Epub 20230316. doi: 10.1161/circresaha.122.321566. PubMed PMID: 36927182; PMCID: PMC10027394.
4. Sloan AR, Lee-Poturalski C, Hoffman HC, Harris PL, Elder TE, Richardson B, Kerstetter-Fogle A, Cioffi G, Schroer J, Desai A, Cameron M, Barnholtz-Sloan J, Rich J, Jankowsky E, Sen Gupta A, Sloan AE. Glioma stem cells activate platelets by plasma-independent thrombin production to promote glioblastoma tumorigenesis. Neuro-Oncology Advances. 2022;4(1). doi: 10.1093/noajnl/vdac172.
5. Liao K, Zhang X, Liu J, Teng F, He Y, Cheng J, Yang Q, Zhang W, Xie Y, Guo D, Cao G, Xu Y, Huang B, Wang X. The role of platelets in the regulation of tumor growth and metastasis: the mechanisms and targeted

therapy. MedComm (2020). 2023;4(5):e350. Epub 20230914. doi: 10.1002/mco2.350. PubMed PMID: 37719444; PMCID: PMC10501337.
6. Sloan AR, Gordillo AJ, Kennemer A, Khorana AA, Horbinski C, Kaelber DC, Cameron SJ, Lathia JD. VTE incidence shortens survival in IDH-WT glioblastoma. medRxiv. 2025. Epub 20250109. doi: 10.1101/2025.01.08.25319908. PubMed PMID: 39830282; PMCID: PMC11741497.
7. Yang J, Yamashita-Kanemaru Y, Morris BI, Contursi A, Trajkovski D, Xu J, Patrascan I, Benson J, Evans AC, Conti AG, Al-Deka A, Dahmani L, Avdic-Belltheus A, Zhang B, Okkenhaug H, Whiteside SK, Imianowski CJ, Wesolowski AJ, Webb LV, Puccio S, Tacconelli S, Bruno A, Di Berardino S, De Michele A, Welch HCE, Yu IS, Lin SW, Mitra S, Lugli E, van der Weyden L, Okkenhaug K, Saeb-Parsy K, Patrignani P, Adams DJ, Roychoudhuri R. Aspirin prevents metastasis by limiting platelet TXA(2) suppression of T cell immunity. Nature. 2025. Epub 20250305. doi: 10.1038/s41586-025-08626-7. PubMed PMID: 40044852.
8. Turaga SM, Silver DJ, Bayik D, Paouri E, Peng S, Lauko A, Alban TJ, Borjini N, Stanko S, Naik UP, Keri RA, Connor JR, Barnholtz-Sloan JS, Rubin JB, Berens M, Davalos D, Lathia JD. JAM-A functions as a female microglial tumor suppressor in glioblastoma. Neuro Oncol. 2020;22(11):1591-601. doi: 10.1093/neuonc/noaa148. PubMed PMID: 32592484; PMCID: PMC7690368.
9. Bayik D, Zhou Y, Park C, Hong C, Vail D, Silver DJ, Lauko A, Roversi G, Watson DC, Lo A, Alban TJ, McGraw M, Sorensen M, Grabowski MM, Otvos B, Vogelbaum MA, Horbinski C, Kristensen BW, Khalil AM, Hwang TH, Ahluwalia MS, Cheng F, Lathia JD. Myeloid-Derived Suppressor Cell Subsets Drive Glioblastoma Growth in a Sex-Specific Manner. Cancer Discov. 2020;10(8):1210-25. Epub 20200416. doi: 10.1158/2159-8290.Cd-19-1355. PubMed PMID: 32300059; PMCID: PMC7415660.
10. Lee J, Nicosia M, Hong ES, Silver DJ, Li C, Bayik D, Watson DC, Lauko A, Kay KE, Wang SZ, Johnson S, McGraw M, Grabowski MM, Kish DD, Desai AB, Goodman WA, Cameron SJ, Okada H, Valujskikh A, Fairchild RL, Ahluwalia MS, Lathia JD. Sex-Biased T-cell Exhaustion Drives Differential Immune Responses in Glioblastoma. Cancer Discov. 2023;13(9):2090-105. doi: 10.1158/2159-8290.Cd-22-0869. PubMed PMID: 37378557; PMCID: PMC10481130.
11. Ostrom QT, Kinnersley B, Wrensch MR, Eckel-Passow JE, Armstrong G, Rice T, Chen Y, Wiencke JK, McCoy LS, Hansen HM, Amos CI, Bernstein JL, Claus EB, Il'yasova D, Johansen C, Lachance DH, Lai RK, Merrell RT, Olson SH, Sadetzki S, Schildkraut JM, Shete S, Rubin JB, Lathia JD, Berens ME, Andersson U, Rajaraman P, Chanock SJ, Linet MS, Wang Z, Yeager M, Houlston RS, Jenkins RB, Melin B, Bondy ML, Barnholtz-Sloan JS. Sex-specific glioma genome-wide association study identifies new risk locus at 3p21.31 in females, and finds sex-differences in risk at 8q24.21. Sci Rep. 2018;8(1):7352. Epub 20180509. doi: 10.1038/s41598-018-24580-z. PubMed PMID: 29743610; PMCID: PMC5943590.
12. Fomchenko EI, Holland EC. Platelet-derived growth factor-mediated gliomagenesis and brain tumor recruitment. Neurosurg Clin N Am. 2007;18(1):39-58, viii. Epub 2007/01/25. doi: 10.1016/j.nec.2006.10.006. PubMed PMID: 17244553.
13. Khorana AA, Mackman N, Falanga A, Pabinger I, Noble S, Ageno W, Moik F, Lee AYY. Cancer-associated venous thromboembolism. Nat Rev Dis Primers. 2022;8(1):11. Epub 20220217. doi: 10.1038/s41572-022-00336-y. PubMed PMID: 35177631.
14. Wang TF, Khorana AA, Agnelli G, Bloomfield D, Bonaca MP, Büller HR, Connors JM, Goto S, Jing ZC, Kakkar AK, Khder Y, Raskob GE, Soff GA, Verhamme P, Weitz JI, Carrier M. Treatment of Cancer-Associated Thrombosis: Recent Advances, Unmet Needs, and Future Direction. Oncologist. 2023;28(7):555-64. doi: 10.1093/oncolo/oyad116. PubMed PMID: 37171998; PMCID: PMC10322141.
15. Sloan AR, Gordillo AJ, Kennemer A, Khorana AA, Horbinski C, Kaelber DC, Cameron SJ, Lathia JD. Venous thromboembolism incidence shortens survival in isocitrate dehydrogenase wild-type glioblastoma. Neurooncol Adv. 2025;7(1):vdaf018. Epub 20250131. doi: 10.1093/noajnl/vdaf018. PubMed PMID: 40264942; PMCID: PMC12012773.
16. Burdett KB, Unruh D, Drumm M, Steffens A, Lamano J, Judkins J, Schwartz M, Javier R, Amidei C, Lipp ES, Peters KB, Lai A, Eldred BSC, Heimberger AB, McCortney K, Scholtens DM, Horbinski C. Determining venous thromboembolism risk in patients with adult-type diffuse glioma. Blood. 2023;141(11):1322-36. doi: 10.1182/blood.2022017858. PubMed PMID: 36399711; PMCID: PMC10082363.
17. Diaz M, Jo J, Smolkin M, Ratcliffe SJ, Schiff D. Risk of Venous Thromboembolism in Grade II-IV Gliomas as a Function of Molecular Subtype. Neurology. 2021;96(7):e1063-e9. Epub 20201222. doi: 10.1212/wnl.0000000000011414. PubMed PMID: 33361259; PMCID: PMC8055337.
18. Unruh D, Horbinski C. Beyond thrombosis: the impact of tissue factor signaling in cancer. J Hematol Oncol. 2020;13(1):93. Epub 2020/07/16. doi: 10.1186/s13045-020-00932-z. PubMed PMID: 32665005; PMCID: PMC7362520.

19. Suzuki K, Aiura K, Kitagou M, Hoshimoto S, Takahashi S, Ueda M, Kitajima M. Platelets counts closely correlate with the disease-free survival interval of pancreatic cancer patients. Hepatogastroenterology. 2004;51(57):847-53. Epub 2004/05/18. PubMed PMID: 15143932.
20. Lin MS, Huang JX, Zhu J, Shen HZ. Elevation of platelet count in patients with colorectal cancer predicts tendency to metastases and poor prognosis. Hepatogastroenterology. 2012;59(118):1687-90. Epub 2012/05/18. doi: 10.5754/hge12277. PubMed PMID: 22591645.
21. Cooke NM, Egan K, McFadden S, Grogan L, Breathnach OS, O'Leary J, Hennessy BT, Kenny D. Increased platelet reactivity in patients with late-stage metastatic cancer. Cancer Med. 2013;2(4):564-70. Epub 2013/10/25. doi: 10.1002/cam4.86. PubMed PMID: 24156029; PMCID: PMC3799291.
22. Han X, Knauss EA, Fuente M, Li W, Conlon RA, LePage DF, Jiang W, Renna SA, McKenzie SE, Nieman MT. A mouse model of the protease-activated receptor 4 Pro310Leu variant has reduced platelet reactivity. J Thromb Haemost. 2024;22(6):1715-26. Epub 20240319. doi: 10.1016/j.jtha.2024.03.004. PubMed PMID: 38508397.
23. In 't Veld S, Wurdinger T. Tumor-educated platelets. Blood. 2019;133(22):2359-64. Epub 2019/03/06. doi: 10.1182/blood-2018-12-852830. PubMed PMID: 30833413.
24. Verheul HM, Jorna AS, Hoekman K, Broxterman HJ, Gebbink MF, Pinedo HM. Vascular endothelial growth factor-stimulated endothelial cells promote adhesion and activation of platelets. Blood. 2000;96(13):4216-21. Epub 2000/12/09. PubMed PMID: 11110694.
25. Nash GF, Turner LF, Scully MF, Kakkar AK. Platelets and cancer. Lancet Oncol. 2002;3(7):425-30. Epub 2002/07/27. doi: 10.1016/s1470-2045(02)00789-1. PubMed PMID: 12142172.
26. Pinedo HM, Verheul HM, D'Amato RJ, Folkman J. Involvement of platelets in tumour angiogenesis? Lancet. 1998;352(9142):1775-7. Epub 1998/12/16. doi: 10.1016/s0140-6736(98)05095-8. PubMed PMID: 9848370.
27. Fomchenko EI, Holland EC. Platelet-derived growth factor-mediated gliomagenesis and brain tumor recruitment. Neurosurg Clin N Am. 2007;18(1):39-58, viii. PubMed PMID: 17244553.
28. Shpacovitch V, Feld M, Hollenberg MD, Luger TA, Steinhoff M. Role of protease-activated receptors in inflammatory responses, innate and adaptive immunity. J Leukoc Biol. 2008;83(6):1309-22. Epub 20080319. doi: 10.1189/jlb.0108001. PubMed PMID: 18347074.
29. Hogan PG, Lewis RS, Rao A. Molecular basis of calcium signaling in lymphocytes: STIM and ORAI. Annu Rev Immunol. 2010;28:491-533. doi: 10.1146/annurev.immunol.021908.132550. PubMed PMID: 20307213; PMCID: PMC2861828.
30. Williams M, Liu ZW, Woolf D, Hargreaves S, Michalarea V, Menashy R, Kooner I, Wilson E. Change in platelet levels during radiotherapy with concurrent and adjuvant temozolomide for the treatment of glioblastoma: a novel prognostic factor for survival. J Cancer Res Clin Oncol. 2012;138(10):1683-8. Epub 2012/05/31. doi: 10.1007/s00432-012-1243-x. PubMed PMID: 22644996.
31. Takemoto A, Okitaka M, Takagi S, Takami M, Sato S, Nishio M, Okumura S, Fujita N. A critical role of platelet TGF-β release in podoplanin-mediated tumour invasion and metastasis. Sci Rep. 2017;7:42186. Epub 2017/02/09. doi: 10.1038/srep42186. PubMed PMID: 28176852; PMCID: PMC5297242.
32. Midorikawa Y, Takayama T, Higaki T, Aramaki O, Teramoto K, Yoshida N, Tsuji S, Kanda T, Moriyama M. High platelet count as a poor prognostic factor for liver cancer patients without cirrhosis. Biosci Trends. 2020;14(5):368-75. Epub 2020/07/28. doi: 10.5582/bst.2020.03230. PubMed PMID: 32713867.
33. Baranyai Z, Jósa V, Tóth A, Szilasi Z, Tihanyi B, Zaránd A, Harsanyi L, Szállási Z. Paraneoplastic thrombocytosis in gastrointestinal cancer. Platelets. 2016;27(4):269-75. Epub 2016/05/03. doi: 10.3109/09537104.2016.1170112. PubMed PMID: 27136385.
34. Wan T, Song J, Zhu D. Cancer-associated venous thromboembolism: a comprehensive review. Thrombosis Journal. 2025;23(1):35. doi: 10.1186/s12959-025-00719-7.
35. Wang TF, Li A, Garcia D. Managing thrombosis in cancer patients. Res Pract Thromb Haemost. 2018;2(3):429-38. Epub 2018/07/27. doi: 10.1002/rth2.12102. PubMed PMID: 30046747; PMCID: PMC6046582.
36. Magnus N, Garnier D, Rak J. Oncogenic epidermal growth factor receptor up-regulates multiple elements of the tissue factor signaling pathway in human glioma cells. Blood. 2010;116(5):815-8. Epub 2010/05/14. doi: 10.1182/blood-2009-10-250639. PubMed PMID: 20462964.
37. Tawil N, Bassawon R, Meehan B, Nehme A, Montermini L, Gayden T, De Jay N, Spinelli C, Chennakrishnaiah S, Choi D, Adnani L, Zeinieh M, Jabado N, Kleinman CL, Witcher M, Riazalhosseini Y, Key NS, Schiff D, Grover SP, Mackman N, Couturier CP, Petrecca K, Suvà ML, Patel A, Tirosh I, Najafabadi H, Rak J. Glioblastoma cell populations with distinct oncogenic programs release podoplanin as procoagulant

extracellular vesicles. Blood Adv. 2021;5(6):1682-94. doi: 10.1182/bloodadvances.2020002998. PubMed PMID: 33720339; PMCID: PMC7993100.
38. Künze G, Isermann B. Targeting biased signaling by PAR1: function and molecular mechanism of parmodulins. Blood. 2023;141(22):2675-84. doi: 10.1182/blood.2023019775. PubMed PMID: 36952648; PMCID: PMC10646804.
39. Li S, Wang W, Lin L, Yang L, Cai Y, Yang X, Zhang T, Xiao C, Yan H, Gao N, Zhao J. Oligosaccharide Blocks PAR1 (Proteinase-Activated Receptor 1)-PAR4-Mediated Platelet Activation by Binding to Thrombin Exosite II and Impairs Thrombosis. Arterioscler Thromb Vasc Biol. 2023;43(2):253-66. Epub 20221215. doi: 10.1161/atvbaha.122.318085. PubMed PMID: 36519467.
40. Bock M, Bergmann CB, Jung S, Biberthaler P, Heimann L, Hanschen M. Platelets differentially modulate CD4(+) Treg activation via GPIIa/IIIb-, fibrinogen-, and PAR4-dependent pathways. Immunol Res. 2022;70(2):185-96. Epub 20211221. doi: 10.1007/s12026-021-09258-5. PubMed PMID: 34932195; PMCID: PMC8917040.
41. Mohme M, Neidert MC. Tumor-Specific T Cell Activation in Malignant Brain Tumors. Front Immunol. 2020;11:205. Epub 20200213. doi: 10.3389/fimmu.2020.00205. PubMed PMID: 32117316; PMCID: PMC7031483.
42. Yang W, Liu S, Mao M, Gong Y, Li X, Lei T, Liu C, Wu S, Hu Q. T-cell infiltration and its regulatory mechanisms in cancers: insights at single-cell resolution. J Exp Clin Cancer Res. 2024;43(1):38. Epub 20240202. doi: 10.1186/s13046-024-02960-w. PubMed PMID: 38303018; PMCID: PMC10835979.
43. Morrell CN, Mix D, Aggarwal A, Bhandari R, Godwin M, Owens P, 3rd, Lyden SP, Doyle A, Krauel K, Rondina MT, Mohan A, Lowenstein CJ, Shim S, Stauffer S, Josyula VP, Ture SK, Yule DI, Wagner LE, 3rd, Ashton JM, Elbadawi A, Cameron SJ. Platelet olfactory receptor activation limits platelet reactivity and growth of aortic aneurysms. J Clin Invest. 2022;132(9). Epub 2022/03/25. doi: 10.1172/jci152373. PubMed PMID: 35324479; PMCID: PMC9057618.
44. Godwin MD, Aggarwal A, Hilt Z, Shah S, Gorski J, Cameron SJ. Sex-Dependent Effect of Platelet Nitric Oxide: Production and Platelet Reactivity in Healthy Individuals. JACC Basic Transl Sci. 2022;7(1):14-25. Epub 20211208. doi: 10.1016/j.jacbts.2021.10.009. PubMed PMID: 35128205; PMCID: PMC8807728.
45. Mulkearns-Hubert EE, Hajdari N, Hong ES, Jacobs AP, Gaboriau A, Giltner S, Tannish G, Kay KE, Wang SZ, LaViolette PS, Silver DJ, Hubert CG, Dhawan A, Lathia JD. Connexin 43 drives glioblastoma cancer stem cell phenotypes through a WNK lysine-deficient protein kinase 1-c-MYC signaling axis. Cell Rep. 2025;44(9):116303. Epub 20250913. doi: 10.1016/j.celrep.2025.116303. PubMed PMID: 40946315; PMCID: PMC12443334.
46. Mumaw MM, de la Fuente M, Arachiche A, Wahl JK, 3rd, Nieman MT. Development and characterization of monoclonal antibodies against Protease Activated Receptor 4 (PAR4). Thromb Res. 2015;135(6):1165-71. Epub 20150409. doi: 10.1016/j.thromres.2015.03.027. PubMed PMID: 25890453; PMCID: PMC4437850.
47. Baruah V, O'Connor CM. The BTK-DDX41 axis of the STING pathway is activated during cytomegalovirus lytic infection. J Virol. 2025;99(10):e0104825. Epub 20250916. doi: 10.1128/jvi.01048-25. PubMed PMID: 40956132; PMCID: PMC12548458.
48. Tan Y, Kempchen TN, Becker M, Haist M, Feyaerts D, Liu J, Toma M, Xiao Y, Su G, Rech AJ, Hölzel M, Fan R, Hickey JW, Nolan GP. SPACEc: a streamlined, interactive Python workflow for multiplexed image processing and analysis. Nat Commun. 2025;16(1):10652. Epub 20251127. doi: 10.1038/s41467-025-65658-3. PubMed PMID: 41309581; PMCID: PMC12660697.
49. Goldsborough T, Philps B, O'Callaghan A, Inglis F, Leplat L, Filby A, Bilen H, Bankhead P. InstanSeg: an embedding-based instance segmentation algorithm optimized for accurate, efficient and portable cell segmentation. arXiv preprint arXiv:240815954. 2024.
50. Rumberger JL, Greenwald NF, Ranek JS, Boonrat P, Walker C, Franzen J, Varra SR, Kong A, Sowers C, Liu CC, Averbukh I, Piyadasa H, Vanguri R, Nederlof I, Wang XJ, Van Valen D, Kok M, Bendall SC, Hollmann TJ, Kainmueller D, Angelo M. Automated classification of cellular expression in multiplexed imaging data with Nimbus. Nat Methods. 2025;22(10):2161-70. Epub 20251008. doi: 10.1038/s41592-025-02826-9. PubMed PMID: 41062826.
51. Van Gassen S, Callebaut B, Van Helden MJ, Lambrecht BN, Demeester P, Dhaene T, Saeys Y. FlowSOM: Using self-organizing maps for visualization and interpretation of cytometry data. Cytometry A. 2015;87(7):636-45. Epub 20150108. doi: 10.1002/cyto.a.22625. PubMed PMID: 25573116.
52. Dominguez Mantes A, Herrera A, Khven I, Schlaeppi A, Kyriacou E, Tsissios G, Skoufa E, Santangeli L, Buglakova E, Durmus EB, Manley S, Kreshuk A, Arendt D, Aztekin C, Lingner J, La Manno G, Weigert M. Spotiflow: accurate and efficient spot detection for fluorescence microscopy with deep stereographic flow

regression. Nat Methods. 2025;22(7):1495-504. Epub 20250606. doi: 10.1038/s41592-025-02662-x. PubMed PMID: 40481364.

53. Virtanen P, Gommers R, Oliphant TE, Haberland M, Reddy T, Cournapeau D, Burovski E, Peterson P, Weckesser W, Bright J, van der Walt SJ, Brett M, Wilson J, Millman KJ, Mayorov N, Nelson ARJ, Jones E, Kern R, Larson E, Carey CJ, Polat İ, Feng Y, Moore EW, VanderPlas J, Laxalde D, Perktold J, Cimrman R, Henriksen I, Quintero EA, Harris CR, Archibald AM, Ribeiro AH, Pedregosa F, van Mulbregt P. Author Correction: SciPy 1.0: fundamental algorithms for scientific computing in Python. Nat Methods. 2020;17(3):352. doi: 10.1038/s41592-020-0772-5. PubMed PMID: 32094914; PMCID: PMC7056641.

Figures and Figure Legends

Figure 1

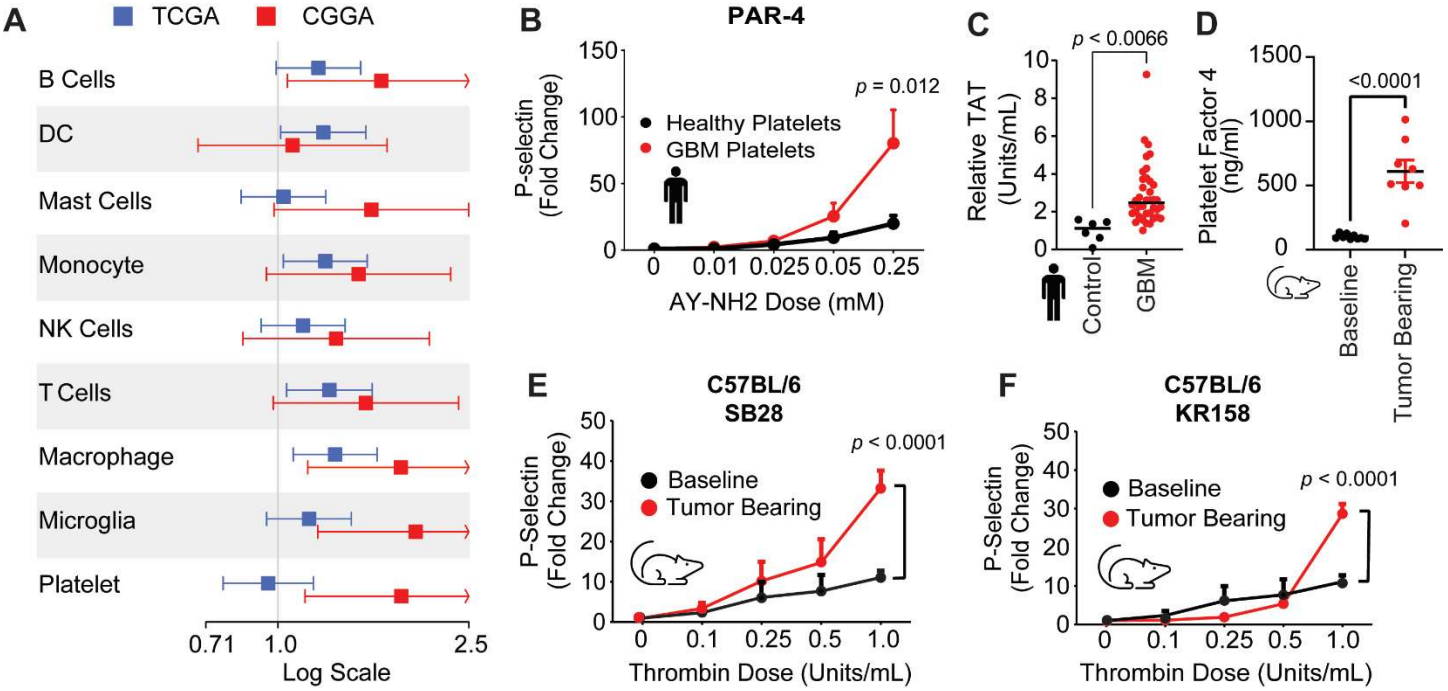

Figure 1. PAR4 signaling drives hyperactive platelets in GBM patients. **A**. WHO grade 4 IDH wildtype GBM samples from the publicly available data sets The Cancer Genome Atlas (TCGA) and Chinese Glioma Genome Atlas (CGGA_325). Univariate Cox proportional hazards models were constructed, and deconvoluted immune cell proportions and platelet signature score were z-score normalized and centered prior to hazard ratio computation. Hazard ratios depicted describe overall survival with 95% confidence intervals as a function of immune cell proportion or platelet signature score. **B**. Washed platelets isolated from patients with a GBM diagnosis and matched control subjects were treated with AY-NH2 to stimulate PAR4, and α-granule secretion was measured using an antibody specific for P-selectin via flow cytometry. Data are represented as means ± SEM from *n*=18 GBM patients and *n*=18 control subjects. Two-way ANOVA was performed. **C**. Thrombin-antithrombin (TAT) expression in plasma from GBM and healthy patient platelets as measured by TAT ELISA. An unpaired student's *t*-test was performed. **D**. Serum was isolated from mice before intracranial tumor implantation (baseline) and following intracranial injection of the murine GBM SB28. Following tumor formation, platelet factor 4 (PF4 was measured via ELISA. An unpaired student's *t*-test was performed. **E-F**. Washed platelets were isolated from mice before intracranial tumor implantation (baseline) and following intracranial injection of the murine GBM SB28 (**E**) and KR158 (**F**). Following tumor formation, washed platelets were isolated, and α-granule secretion was measured using an antibody specific for P-selectin via flow cytometry. Data are represented as means ± SEM from n=4 independent experiments. Two-way ANOVA was performed.

Figure 2

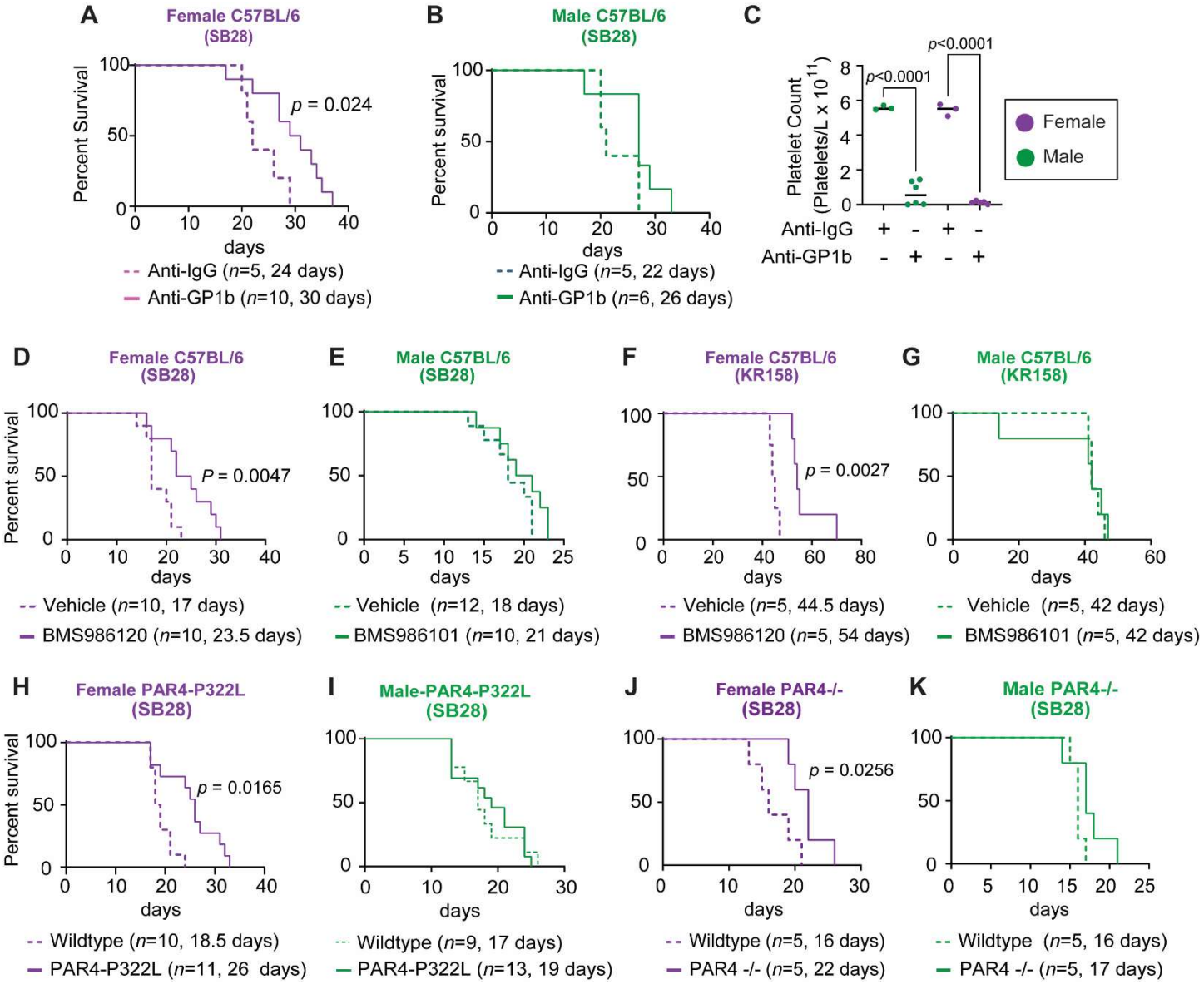

Figure 2. Inhibiting platelets via the thrombin-PAR4 signaling axis prolongs survival in a sex-dependent manner. A, **B**. Kaplan-Meier survival analysis was performed after intracranial tumor implantation of mouse GBM cell model SB28 in C57BL/6 female (**A**) and male (**B**) mice treated with anti-GP1bα depleting antibody. Statistical significance for survival analysis was determined by log-rank test. **C**. Complete blood count (CBC) platelet reading 1 day post anti-GP1bα treatment to validate platelet depletion in the tumor-bearing mice used in panels A and B. Data are shown with each point representing an individual animal. One-way ANOVA analysis with Tukey's multiple comparison test was performed. **D-G**. Kaplan-Meier survival analysis was performed after intracranial transplantation of the mouse GBM cell models SB28 (**D, E**) and KR158 (**F, G**) in immunocompetent C57BL/6 mice followed by pharmacologically inhibiting the thrombin-PAR4 signaling axis by administering BMS986120 (2 mg/kg), a selective PAR4 inhibitor. Statistical significance for survival analysis was determined by log-rank test. **H**, **I.** Kaplan-Meier survival analysis comparing female (**H**) and male (**I**) C57BL/6 wildtype and C57BL/6 - PAR-P322L mice following intracranial transplantation of the mouse GBM cell model SB28. Statistical significance for survival analysis was determined by log-rank test. **J**, **K.** Kaplan-Meier survival analysis comparing female (**J**) and male (**K**) C57BL/6 wildtype and C57BL/6-PAR4-/- mice following intracranial transplantation of the mouse GBM cell model SB28. Statistical significance for survival analysis was determined by log-rank test.

005 **Figure 3**

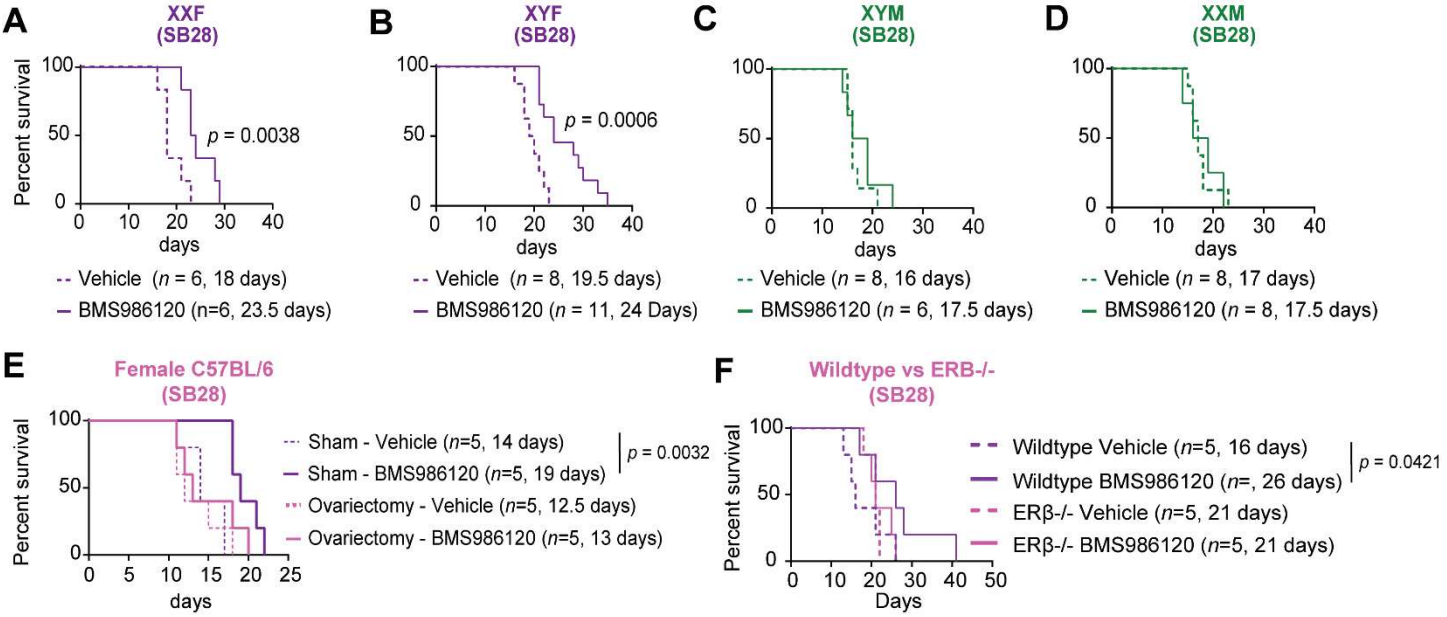

006

007 **Figure 3. Inhibiting the thrombin-PAR4 signaling axis prolongs survival in a female estrogen-specific**
008 **manner. A-D.** Kaplan-Meier survival analysis was performed after intracranial transplantation of the mouse GBM
009 cell model SB28 and treatment with BMS986120. The four core genotype model results in (**A**) wildtype female,
010 (**B**) chromosomal male (XY)-hormonal female mice, (**C**) wildtype male, and (**D**) chromosomal female (XX)-
011 hormonal male mice. Statistical significance for survival analysis was determined by log-rank test. **E**. Survival
012 analysis of C57BL/6 female mice who underwent an ovariectomy or sham procedure and were intracranially
013 transplanted with SB28 cells 30 days post ovariectomy and subsequently treated with BMS986120 (2 mg/kg).
014 Statistical significance for survival analysis was determined by log-rank test. **F**. Kaplan-Meier survival analysis
015 comparing female C57BL/6 wildtype and C57BL/6 – Erβ-/- mice following intracranial transplantation of the
016 mouse GBM cell model SB28. Statistical significance for survival analysis was determined by log-rank test.
017

018

019

Figure 4

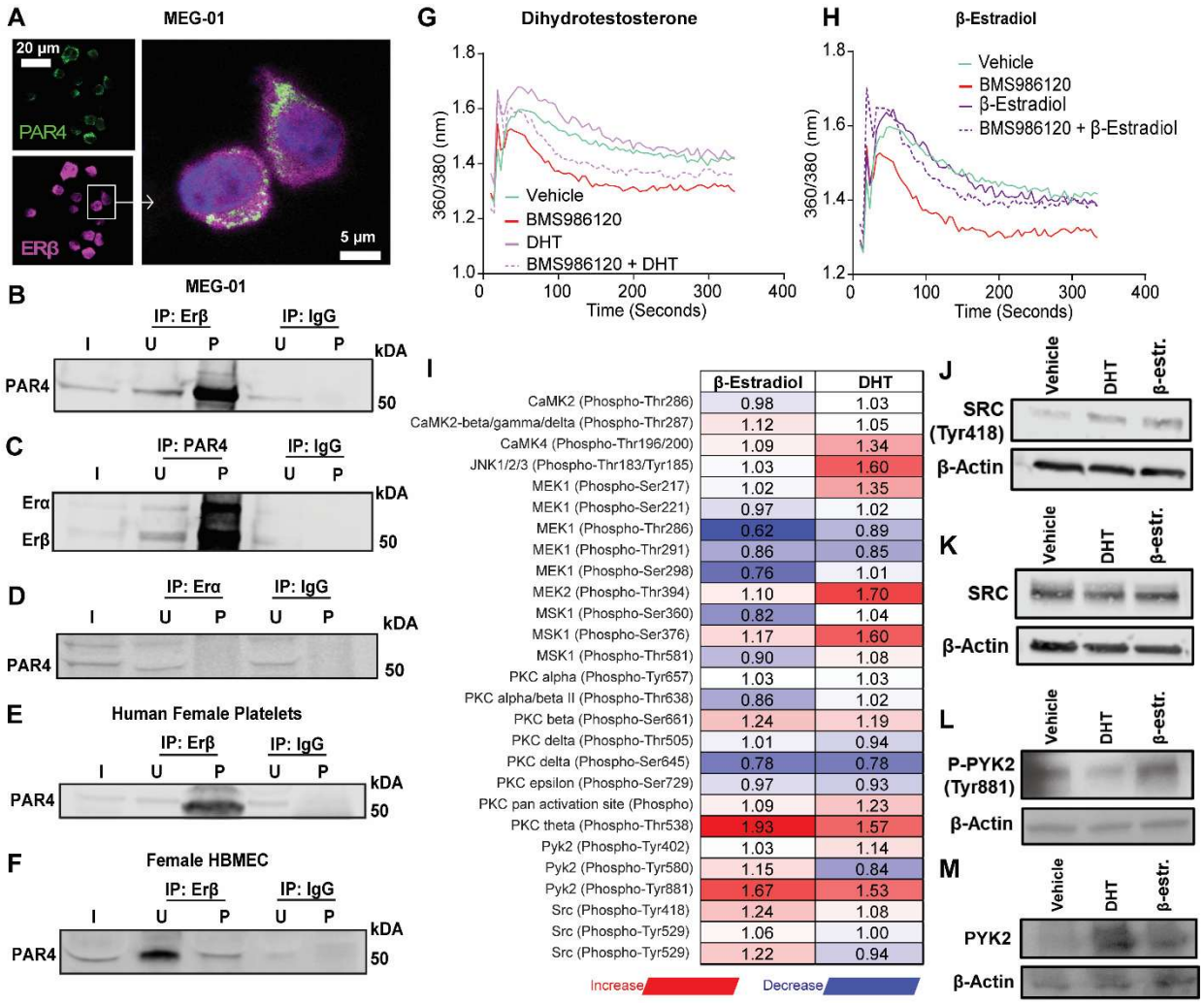

Figure 4. Estrogen receptor-β interacts with and regulates PAR4 signaling. A. Immunofluorescence (IF) staining of MEG-01 cells; IF staining of PAR4, Erβ. Merged image of DAPI, PAR4, and Erβ IF staining (Scale = 20 µm). **B.** Immunoprecipitation of Erβ and IgG followed by immunoblotting for PAR4 in MEG-01 cells. **C.** Immunoprecipitation of PAR4 and IgG followed by immunoblotting for Erβ in MEG-01 cells. **D.** Immunoprecipitation of Erα and IgG followed by immunoblotting for PAR4 in MEG-01 cells. **E.** Immunoprecipitation of Erβ and IgG followed by immunoblotting for PAR4 in human female platelets. F**.** Immunoprecipitation of PAR4 and IgG followed by immunoblotting for Erβ in human brain microvascular endothelial cells. **G**, **H**. Fura-2 calcium imaging of MEG-01 cells pretreated with BMS986120 and either (**G**) dihydrotestosterone or (**H**) β-estradiol followed by stimulation with thrombin. **I**. G protein-coupled receptor (GPCR) phospho-array of MEG-01 cells treated with β-estradiol or testosterone for 4 consecutive days. GPCR phospho-array was conducted and analyzed in collaboration with Full Moon Bio. Data represented as fold change relative to MEG-01 cells treated with vehicle. **J-M**. Validation of the GPCR phospho-array. MEG-01 cells were treated with β-estradiol or testosterone for 4 consecutive days, and lysates were immunoblotted for phospho-SRC (Tyr418) (**J**), SRC (**K**), phospho-PYK2 (Tyr881) (**L**), and PYK2 (**M**). Actin was used as a loading control.

041 **Figure 5**

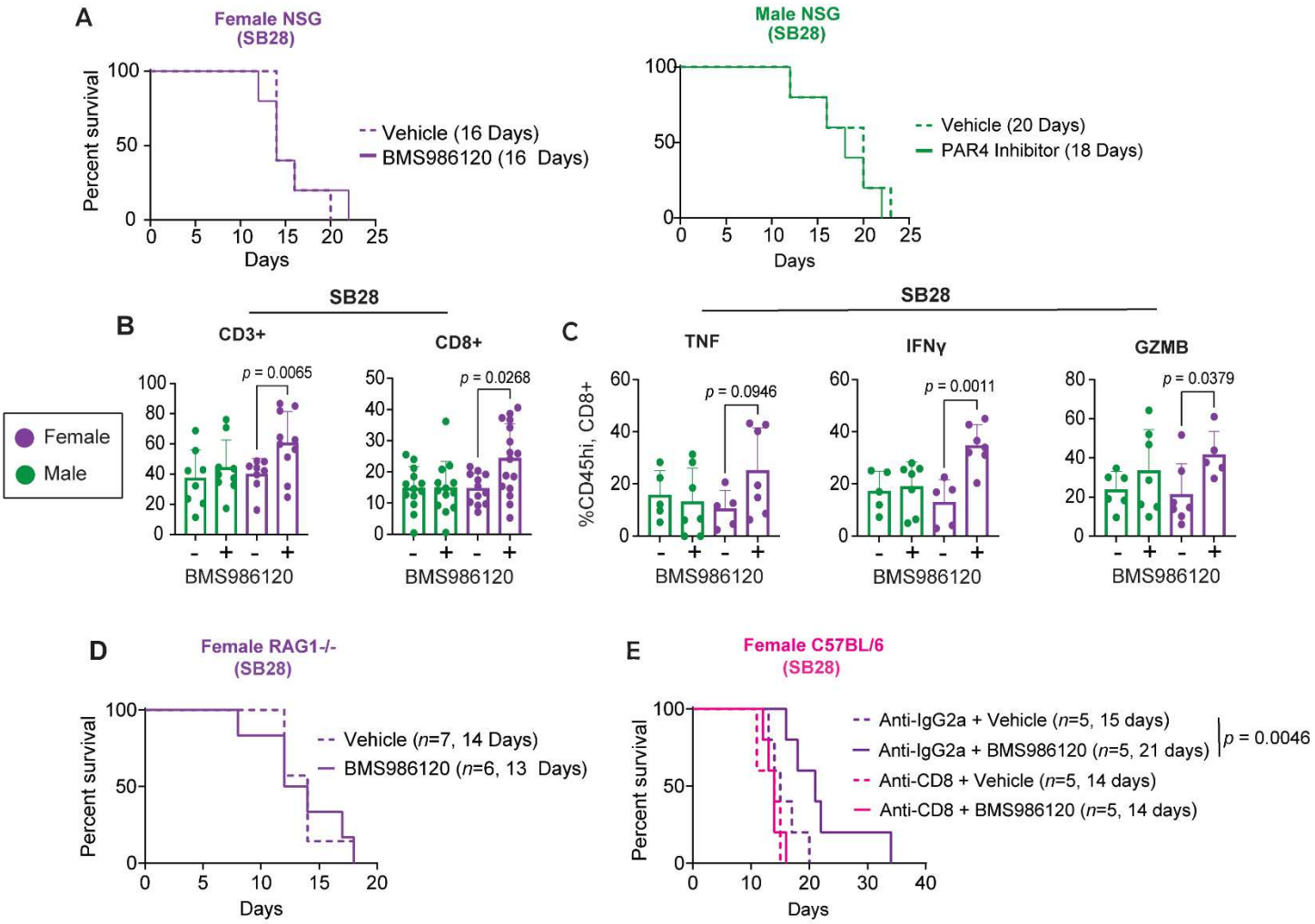

042

043 **Figure 5. Inhibiting thrombin-PAR4 signaling enhances CD8+ T cells in a sex-dependent manner**. **A.**
044 Kaplan-Meier survival analysis was performed after intracranial injection of the mouse GBM cell model SB28 in
045 immunodeficient NSG mice followed by pharmacologically inhibiting the thrombin-PAR4 signaling axis by
046 administering BMS986120 (2 mg/kg), a selective PAR4 inhibitor. Statistical significance for survival analysis was
047 determined by log-rank test. **B**. Frequency of tumor-infiltrating T-cell subsets 14 days post intracranial
048 implantation of SB28 in male and female C57BL/6 mice treated with and without BMS986120. Data are combined
049 from two independent experiments. One-way ANOVA analysis with Tukey's multiple comparison test was
050 performed. **C**. Intracellular cytokine expression in tumor-infiltrating CD8+ T cells. Data are combined from two
051 independent experiments. One-way ANOVA analysis with Tukey's multiple comparison test was performed. **D**.
052 Kaplan-Meier survival curve depicting survival of SB28-bearing *Rag1-/-* female mice treated with BMS986120.
053 Statistical significance for survival analysis was determined by log-rank test. **E**. Kaplan-Meier survival curve
054 depicting survival of SB28 tumor-bearing females treated with anti-CD8-depleting antibody with BMS986120
055 administration. Statistical significance for survival analysis was determined by log-rank test.).

056

Figure 6

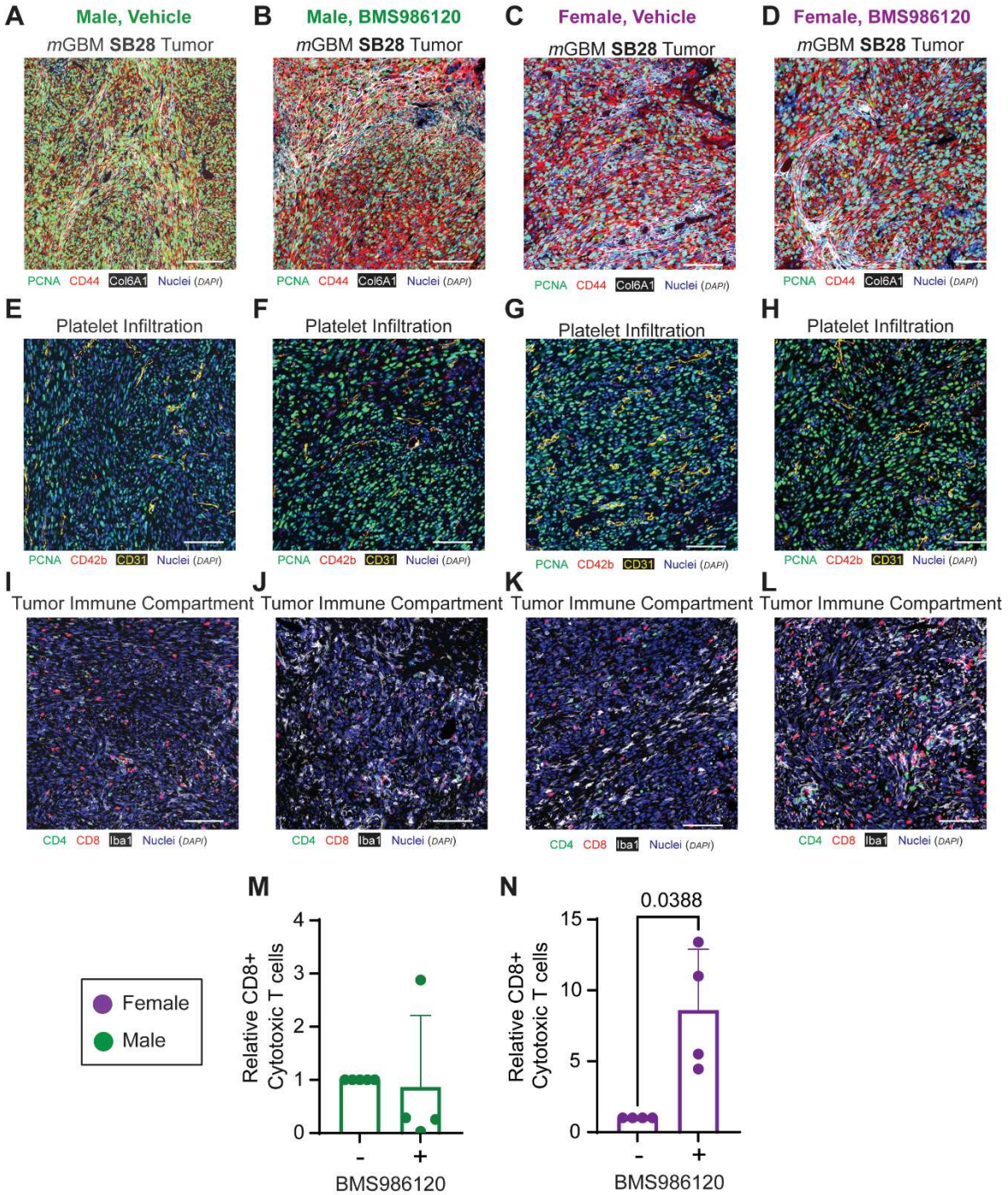

Figure 6. Inhibiting PAR4 increases intratumoral CD8+ T cells and decreases intratumoral platelets in tumor bearing mice. A-D. Akoya multispectral immunofluorescence imaging analysis of Merged image of DAPI, PCNA, CD44, and Col6A1 in (**A**) male vehicle treated, (**B**) male BMS986120 treated, (**C**) female vehicle treated, and (**D**) female BMS986120 treated. **E-H**. Akoya multispectral immunofluorescence imaging analysis of Merged image of DAPI, CD42b (platelet), CD31, and PCNA in (**E**) male vehicle treated, (**F**) male BMS986120 treated, (**G**) female vehicle treated, and (**H**) female BMS986120 treated. **I-L.** Akoya multispectral immunofluorescence imaging analysis of Merged image of DAPI, CD4, CD8, and Iba1 in (**I**) male vehicle treated, (**J**) male BMS986120 treated, (**K**) female vehicle treated, and (**L**) female BMS986120 treated. **M-N**. Akoya multispectral immunofluorescence quantification of CD8+ cytotoxic T cells from SB28 tumor bearing (**M**) male and (**N**) female vehicle and BMS986120 treated mice. An unpaired student's *t*-test was performed.

Figure 7

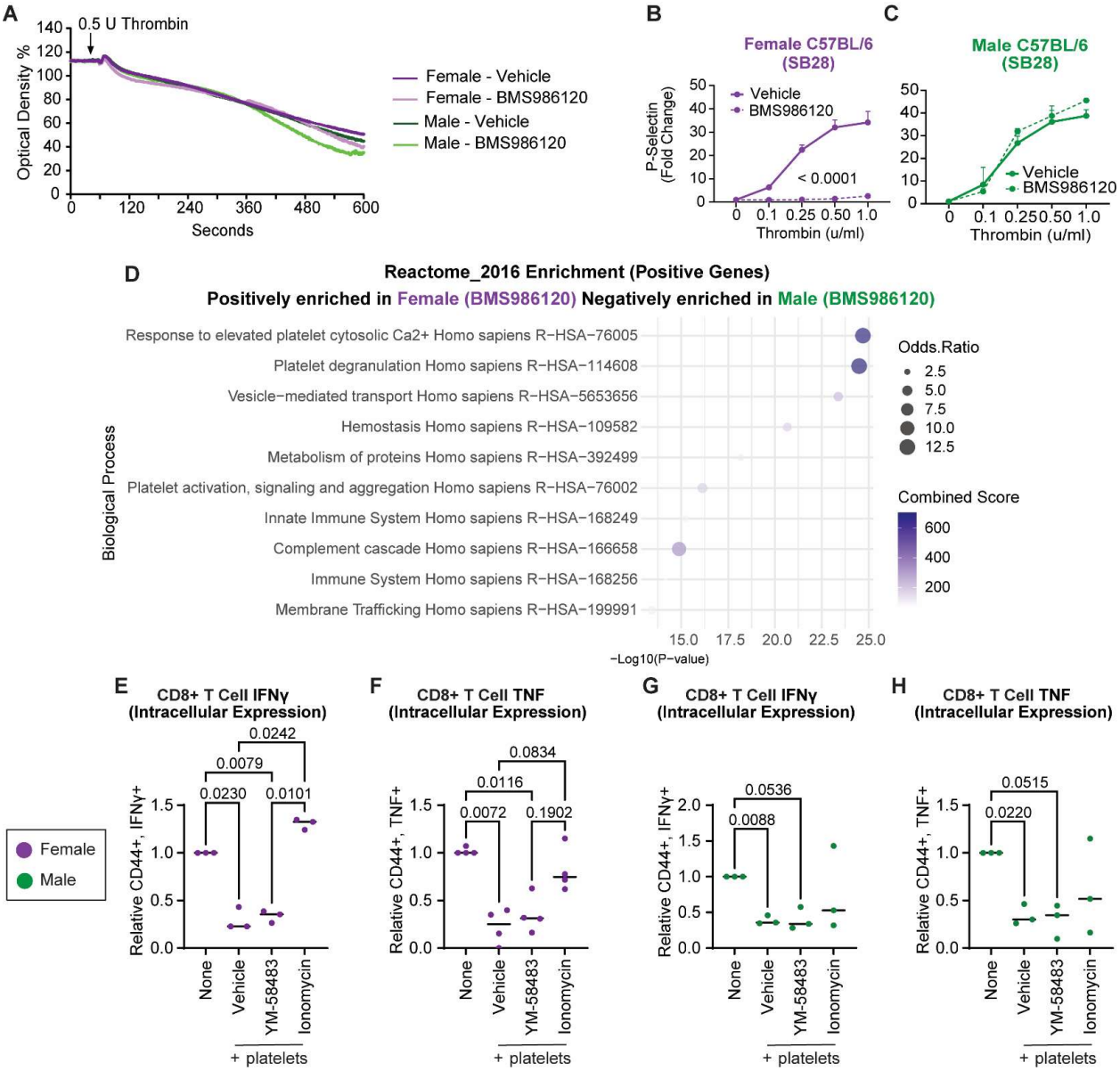

Figure 7. Inhibiting PAR4 enhances Ca^{2+} signaling, platelet secretion and exocytosis in a sex-dependent manner. A. Aggregometry analysis of washed platelets isolated from mice treated with BMS986120 following intracranial implantation of SB28 and stimulated with 0.5 U thrombin. Statistical significance was determined by a two-way ANOVA. **B, C.** Washed platelets isolated from mice treated with BMS986120 following intracranial implantation of SB28. Washed platelets were isolated, and α-granule secretion was measured using an antibody specific for P-selectin. Data are represented as means ± SEM. Statistical significance was determined by two-way ANOVA. **D**. Proteomic GO enrichment analysis of washed platelets isolated from mice treated with BMS986120 following intracranial implantation of SB28. Pathways are positively enriched in female BMS986120 platelets and negatively enriched in male BMS986120 platelets. **E-H**. Intracellular cytokine expression of CD8+ T cells isolated from (**E**, **F**) female and (**G**, **H**) male C57BL/6 mouse spleens and co-cultured with sex-matched washed platelets isolated from B6 wildtype mice; platelets were pre-treated with vehicle, YM-58483, or ionomycin before addition to platelets, fresh platelets were added for 3 consecutive days, and intracellular IFNγ (**E, G**) and TNF (**F**, **H**) expression was measured by flow cytometry. One-way ANOVA analysis with Tukey's multiple comparison test was performed.

Figure 8

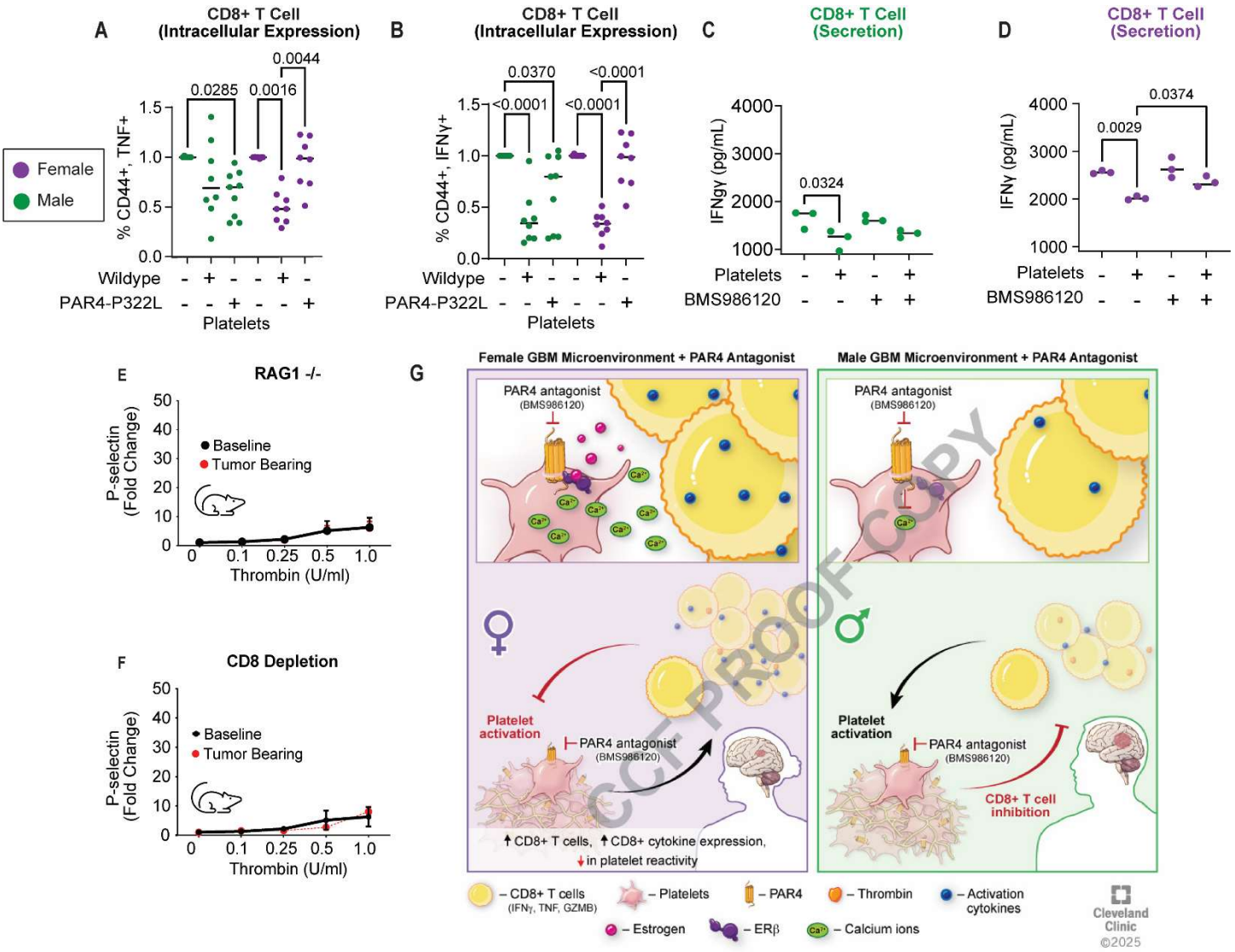

Figure 8. Bidirectional regulation between platelets and CD8+ T cells in GBM. A, B. Intracellular cytokine expression of CD8+ T cells isolated from C57BL/6 mouse spleen and co-cultured with sex-matched washed platelets isolated from C57BL/6 mice or PAR4-P322L mice; fresh platelets were added for 3 consecutive days, and intracellular TNF (**A**) and IFNγ (**B**) expression was measured by flow cytometry. One-way ANOVA analysis with Tukey's multiple comparison test was performed. **C, D**. IFNγ cytokine secretion from male (**C**) and female (**D**) CD8+ T cells isolated from C57BL/6 mouse spleen and co-cultured with sex-matched washed platelets isolated from C57BL/6 mice; fresh platelets were added for 3 consecutive days, and supernatant IFNγ secretion was measured by ELISA. One-way ANOVA analysis with Tukey's multiple comparison test was performed. **E, F**. Washed platelets isolated from *Rag1-/-* mice (**E**) and C57BL/6-CD8-depleted mice (**F**) before intracranial tumor implantation (baseline) and two weeks following intracranial injection of SB28 cells. Washed platelets were isolated, and α-granule secretion was measured using an antibody specific to P-selectin via flow cytometry. Data are represented as means ± SEM from n=4 independent experiments. **G**. Proposed model where platelet-mediated PAR4 signaling is as a critical driver of tumor progression and identifying sex-specific immune responses as key to therapeutic efficacy.